AGU ADVANCING EARTH AND SPACE SCIENCE

JGR Solid Earth

RESEARCH ARTICLE

10.1029/2021JB023165

Key Points:

- Weak high-temperature remanence components discriminated by using a furnace with ultra-low residual magnetic field
- Self-reversed remanence carried by Al-substituted hematite with unblocking temperature of around 640°C
- Self-reversal of chemical magnetic remanence recorded on the transformation from Al-substituted maghemite to Al-substituted hematite

Supporting Information:

Supporting Information may be found in the online version of this article.

Correspondence to:

C. Liu,
liucaicai@126.com;
liucaicai@ies.ac.cn

Citation:

Liu, C., Qin, H., Ferré, E. C., Wang, W., He, K., & Deng, C. (2022). Importance of hematite self-reversal in Al-rich soils magnetostratigraphy: Revisiting the Damei red soil sequence in the Bose Basin, southern China. *Journal of Geophysical Research: Solid Earth*, *127*, e2021JB023165. https://doi.org/10.1029/2021JB023165

Received 3 SEP 2021
Accepted 21 MAR 2022

Importance of Hematite Self-Reversal in Al-Rich Soils Magnetostratigraphy: Revisiting the Damei Red Soil Sequence in the Bose Basin, Southern China

Caicai Liu[1], Huafeng Qin[2], Eric C. Ferré[3], Wei Wang[4], Kuang He[5,6], and Chenglong Deng[2]

[1]State Key Laboratory of Earthquake Dynamics, Institute of Geology, China Earthquake Administration, Beijing, China, [2]State Key Laboratory of Lithospheric Evolution, Institute of Geology and Geophysics, Chinese Academy of Sciences, Beijing, China, [3]School of Geosciences, University of Louisiana at Lafayette, Lafayette, LA, USA, [4]Institute of Cultural Heritage, Shandong University, Qingdao, China, [5]Key Laboratory of Earth and Planetary Physics, Institute of Geology and Geophysics, Chinese Academy of Sciences, Beijing, China, [6]Frontiers Science Center for Deep Ocean Multispheres and Earth System, Key Laboratory of Submarine Geosciences and Prospecting Techniques, MoE and College of Marine Geosciences, Ocean University of China, Qingdao, China

Abstract Understanding the acquisition of chemical remagnetization that commonly takes place in sedimentary red beds is crucial not only to assess the stability of primary chemical remanent magnetization (CRM) but also to evaluate the impact of diagenesis on the paleomagnetic record. The inconsistency between the magnetostratigraphy and the 0.803 Ma age of tektites within the upper vermiculated unit of a red soil sequence (Damei) in southern China strongly suggests pervasive remagnetization. This remagnetization has previously been interpreted as a CRM lock-in. However, our recent study suggests that the upper soil units of this section above the tektite-bearing layer have experienced milder weathering than the underlying layer. It seems that CRM lock-in has not completely overprinted the primary remanence of this section. To investigate the exact remagnetization mechanism, the magnetostratigraphy of the Damei sequence was revisited and the oriented samples were subjected to progressive thermal demagnetization up to 680°C (instead of 585°C in our previous study) by using a newly designed oven with ultralow magnetic field noise. The new demagnetization results for vermiculated and red clay samples document a high-temperature (HT) remanence component above 630°C with some above 525°C, and a self-reversal medium temperature (MT) component between 300 and 585°C. The magnetic polarities of most HT components are consistent with the tektite age. The self-reversal MT component is carried by Al-substituted hematite transformed from Al-substituted maghemite. Self-reversal likely occurred during the maghemite to hematite transformation process. Additional attention should be paid when using magnetostratigraphy to date highly weathered aluminum-rich red sediments.

Plain Language Summary The information of the paleomagnetic field is crucial to understand the evolution of the geomagnetic field. Sediments are important carriers of paleomagnetic signals. Red beds, as a volumetrically significant type of sediment, are widely distributed in tropical and subtropical regions. The warm or hot climate in these areas favors the formation of red or brown iron oxides, such as hematite and maghemite, the former being always the main pigments of red beds. These iron oxides always carry a chemical remanent magnetization (CRM), which records the direction of the geomagnetic field when these minerals form. This type of CRM usually partially or completely overprints the detrital remanent magnetization (DRM) that was recorded when the red beds formed, and thus complicates paleomagnetic interpretations. In this study, by using a new thermal demagnetizer designed to have an ultralow magnetic noise, the weak DRM components of a strongly weathered red soil sequence have been successfully discriminated against despite being partially overprinted by CRM. This study revises the previous magnetostratigraphy which was only based on the CRM components. Our results suggest that additional attention should be paid when getting paleomagnetic information from highly weathered red sediments.

1. Introduction

Most red beds accumulated between north and south latitudes of 30° which define tropical and subtropical regions (Van Houten, 1973; Walker, 1967, 1974). These deposits have long been considered as an indicator of a specific climate with an oxidizing environment (e.g., Glennie, 1970; Millot et al., 1970; Van Houten, 1973). Studies of modern and ancient deserts show the pigmentation of red beds was favored by a hot, dry climate

10.1029/2021JB023165

Figure 1. Schematic map showing the distribution of the Damei, Xuancheng (XC), and Qiliting (QLT) sections.

(e.g., Walker, 1967), while red sediments in savannas and floodplains bear a warm, moist climate (e.g., Jones, 1965; Oliver & Prave, 2013). Under these climatic conditions, iron oxides, such as hematite and goethite, are always the main pigments of red beds (Van Houten, 1973). These pigment minerals usually come from in situ alterations of iron silicates and other iron-bearing detrital grains. This alteration process develops during or after accumulation by weathering, which is significantly influenced by climatic intensity (Ruhe, 1967). If these pigments acquire remanent magnetization when they formed, the magnetic remanence should be attributed to chemical remanent magnetization (CRM), which makes a great contribution to the natural remanent magnetization (NRM) of red beds (Collinson, 1965, 1966).

The presence of CRM in NRM always causes complexity to decipher the signal of magnetic field recorded in red beds when they were deposited, because CRM is usually superimposed onto a primary detrital remanent magnetization (DRM) and sometimes partially or even totally overprints DRM (e.g., Collinson, 1966, 1974; Jiang et al., 2017; Liu, Ge, et al., 2011; Tauxe et al., 1980). Understanding the formation mechanism of CRM not only helps to correctly explain the paleomagnetic records in red beds but also is useful to investigate the postdepositional process (Jiang et al., 2022; Liu et al., 2010; Yuan et al., 2021). In this study, we try to find this mechanism by investigating the paleomagnetic records of a red soil sequence (Damei) in subtropical southern China which was believed to be remagnetized by CRM (Deng et al., 2007).

The Damei sequence is located near the Tropic of Cancer (Figure 1). Our previous work (Liu et al., 2010) suggested that a special type of pedogenic hematite with lower unblocking temperature (T_B) but higher coercivity compared with detrital hematite, is the main carrier of secondary CRM of this section. This CRM is strong enough to mask the primary DRM and caused the inconsistency between magnetostratigraphy and $^{40}Ar/^{39}Ar$ age of the tektites (Figure 2a) (Deng et al., 2007; Hou et al., 2000). We previously explained this phenomenon as a large lock-in depth (>4 m) of CRM (Deng et al., 2007). That means a weathering process happened later than the Matuyama-Brunhes boundary (at least above the depth of 3.2 m, the upper boundary of the tektite layer; Figure 2a) should be sufficiently strong to form enough pedogenic hematite in the whole section which record the normal polarity of the Brunhes chron. However, geochemical indexes and environmental magnetic parameters (Liu et al., 2021) (Figure 2a) indicate that the weathering above the tektite layer was weaker than that below. The later weak weathering unlikely altered the pedogenic minerals which have been oxidized in an early strong pedogenic process. For example, most hematite particles in the Damei sequence are pedogenic, as suggested by the positive correlation between hematite content and in-situ weathering intensity (Liu et al., 2021). If the pedogenic hematite is formed by late weathering, its content will be higher in the upper units. In contrary, the hematite content is higher in the lower units than in the upper one, as suggested by two lines of evidence: (a) higher "hard" isothermal remanent magnetization (HIRM) and (a) I_{535nm} (the amplitudes of the bands between the minimum at approximately 535 nm and the maximum at approximately 580 nm [characteristic bands of hematite] on the second-derivative diffuse reflectance spectroscopy [DRS]) values in the lower units (Figure 2a). This supports that pedogenic hematite particles were not likely formed by later weathering above the tektite layer but probably produced by syn-depositional pedogenesis.

It seems that the lock-in process caused by late weathering is not the remagnetization mechanism of the Damei sequence. In our previous work, we noticed that the remanent magnetization nearly reached zero when thermally demagnetized to 585°C, which is lower than the T_B of pigment hematite (630–640°C), the main CRM carrier (Liu et al., 2010). Although this can be caused by a wide grain size distribution of pedogenic hematite, this also can result from the mixture of two anti-paralleled remanence components. To find the reason, we carried out detailed progressive thermal demagnetization up to a maximum temperature of 685°C, which is the T_B of well-crystallized hematite. Moreover, we supplemented samples from the units above the vermiculated layer. Detailed rock magnetic analyses have also been carried out to identify magnetic minerals and remanence carriers.

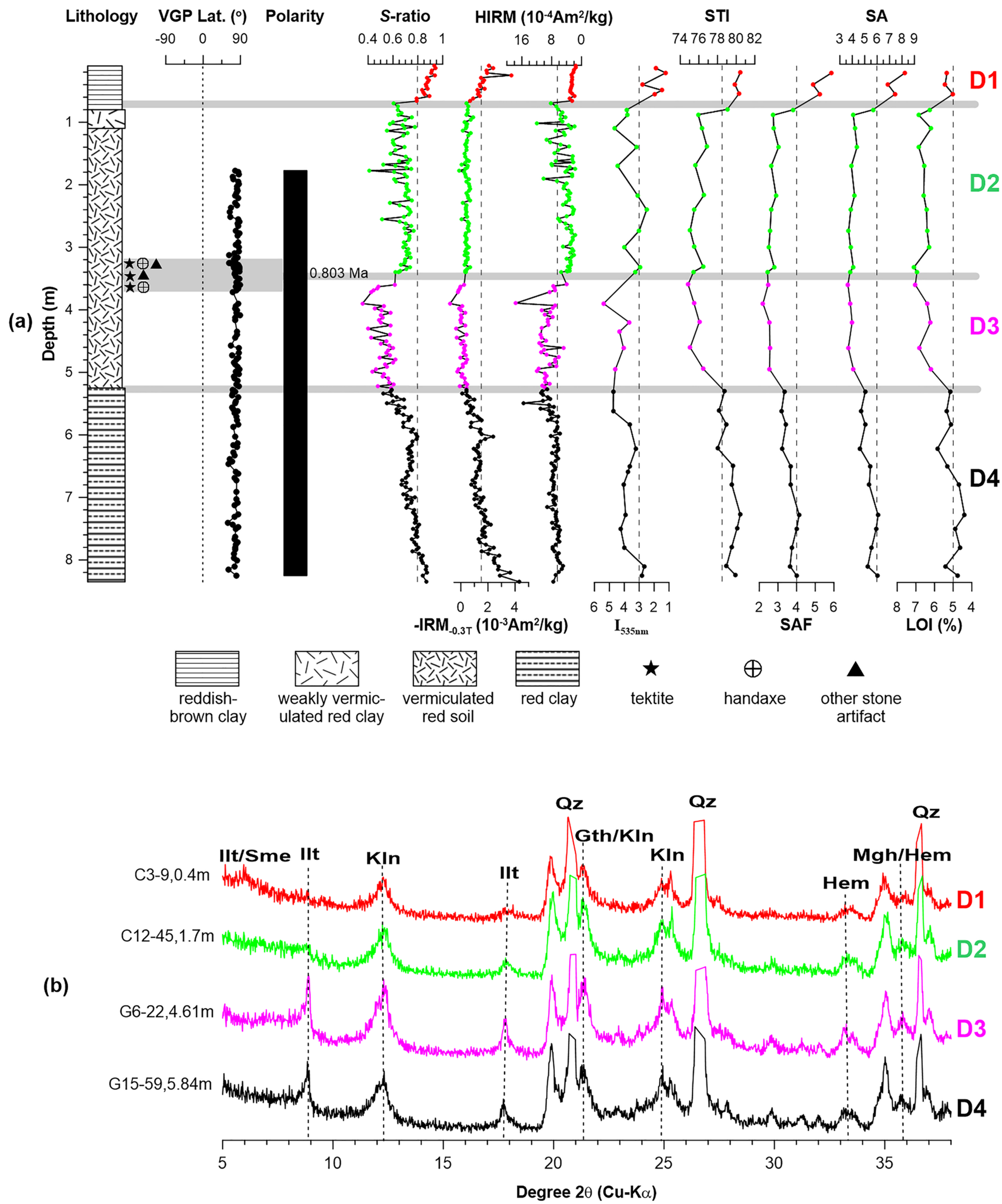
Lithology
VGP Lat. (°)
Polarity
S-ratio
HIRM (10⁻⁴Am²/kg)
STI
SA
D1
D2
D3
D4
0.803 Ma
(a)
Depth (m)
-IRM-0.3T (10⁻³Am²/kg)
I535nm
SAF
LOI (%)
reddish-brown clay
weakly vermiculated red clay
vermiculated red soil
red clay
tektite
handaxe
other stone artifact
(b)
C3-9,0.4m
C12-45,1.7m
G6-22,4.61m
G15-59,5.84m
Ilt/Sme
Ilt
Kln
Qz
Gth/Kln
Hem
Mgh/Hem
Degree 2θ (Cu-Kα)

Figure 2.

2. Setting and Sampling

The Damei red soil sequence (23°46.664′N, 106°43.720′E; Figure 1) is located in the Bose Basin of Guangxi Province in the south of China (Deng et al., 2007; Wang et al., 2008, 2014). The Youjiang River dissects the basin from northwest to southeast. Quaternary sediments form terraces of this river. The Damei sequence consists of fluvial sediments on terrace T4. The sequence sampled in this study can be subdivided into four pedostratigraphical units listed from top to bottom (Figure 2a): (a) reddish-brown clay (0.1–0.8 m); (b) weakly vermiculated red clay (0.8–1.1 m); (b) vermiculated red clay with thick vermiculated structures (1.1–5.25 m); (c) red clay (5.25–8.35 m). Famous Bose Acheulean-like handaxes and other stone artifacts as well as the Australasian tektites have been unearthed at the depth interval of 3.2–3.7 m (Wang et al., 2008).

A few vermiculated red soil samples were obtained from the Xuancheng and Qiliting sequences, which record reliable geomagnetic polarities, along the lower reaches of the Yangtze River (Liu et al., 2008, 2010).

3. Methods

3.1. Paleomagnetic Measurements

Progressive thermal demagnetization (22 steps) up to a maximum temperature of 685°C was carried out on oriented 20 mm cubic samples. The temperature interval was 25–50°C below 585 and 10°C above 585°C. The thermal demagnetizer TD-PGL-100 (designed by the Paleomagnetism and Geochronology Laboratory of the Institute of Geology and Geophysics, Chinese Academy of Sciences), with a residual field of less than 1 nT in the sample zone (Qin et al., 2020), was used. Selected samples were subject to alternating field (AF) demagnetization with a maximum AF field of 100 mT and an interval of 5–10 mT. Paleomagnetic measurements were made using a 2G Enterprises Model 760 cryogenic magnetometer situated in a magnetically shielded room with residual fields smaller than 300 nT.

3.2. High-Temperature Magnetic Measurements

High-temperature magnetic susceptibility measurements ($\chi-T$ curves) were made in our previous work (Liu et al., 2020). In this study, we reanalyzed these curves by calculating the first-order derivative of susceptibility ($d\chi/dT$) and inverse susceptibility $1/\chi$ to better identify contained minerals.

High-temperature magnetization measurements (M_s–T curves) were performed in air using a magnetometer variable field translation balance. A 500 mT magnetic field was applied when samples were continuously heated from room temperature to 700°C and then back to room temperature. The extrapolation method (Moskowitz, 1981) was used to identify the highest T_c.

3.3. Thermal Demagnetization of Three-Component IRM

Three-component (low-coercivity or soft component, medium-coercivity component, and high-coercivity or hard component) IRM was acquired by magnetizing cubic samples in successively smaller fields (2.7, 0.5, and 0.05 T) along with three perpendicular directions (Lowrie, 1990). This composite IRM was then subjected to progressive thermal demagnetization (23 steps) up to 690°C at 10–50°C intervals using a 2G Enterprises Model 760 cryogenic magnetometer.

Another set of sister samples or neighboring samples obtained a three-component IRM and then subjected to a 60 mT three-axis alternating field (AF) demagnetization followed by a progressive thermal demagnetization measurement (23 steps) up to 690°C at 10–50°C intervals. The remanence of each axis was measured before the AF demagnetization.

Figure 2. (a) Lithostratigraphy, magnetic polarity stratigraphy in previous work (Deng et al., 2007), S-ratio (a measure of the relative amounts of high-coercivity minerals to low-coercivity minerals, $0.5 \times [1 - (IRM_{-0.3T}/SIRM)]$), -$IRM_{-0.3T}$ (the absolute amount of low-coercivity [<0.3 T] remanence), HIRM (the absolute amount of high-coercivity remanence), chemical weathering indices of STI ($100*[(SiO_2/TiO_2)/(SiO_2/TiO_2) + (SiO_2/Al_2O_3) + (Al_2O_3/TiO_2)]$), SA ($SiO_2/Al_2O_3$) and SAF ($SiO_2/(Al_2O_3 + Fe_2O_3)$), and loss on ignition (LOI) variations of the Damei red soil sequence (Liu et al., 2020, 2021). Four stages (D1, D2, D3, and D4) of weathering intensity of this sequence have been found. Red, green, pink, and black colors respectively correspond to different weathering stages. (b) XRD spectra of selected samples from these four weathering stages. Ilt, illite; Sme, smectite; Kln, kaolinite; Qz, quartz; *G*th, goethite; Hem, hematite; Mgh, maghemite.

10.1029/2021JB023165

3.4. Acquisition Curves of Isothermal Remanent Magnetization

Selected samples were first demagnetized in alternating fields up to 500 mT and then were imparted an IRM in applied fields from 0 to 2 T, using a vibrating sample magnetometer (VSM MicroMag 3900, Princeton Measurements Corporation). A cumulative log Gaussian analysis (Egli, 2003, 2004; Kruiver et al., 2001; Robertson & France, 1994) was performed to identify magnetic coercivity components. The MAG-MIX package (Egli, 2003, 2004) was used to unmix the data. The logarithmic IRM gradient is also called as coercivity spectrum which can be used to get the information of the amount, type, and grain size of each magnetic mineral present in the sample (Spassov et al., 2003).

3.5. Nonmagnetic Methods

X-ray diffraction (XRD) patterns were obtained from a DMAX2400 X-ray diffractometer to examine mineral assemblages. Diffuse reflectance spectra (DRS) were acquired using a Varian Cary 5000 spectrophotometer (made in California, USA) to semi-quantify hematite and goethite.

Transmission electron microscope (TEM) imaging and selected-area electron diffraction (SAED) patterns were observed with a JEOL JEM-2100 microscope. Elemental analysis was conducted using Oxford X-MAX energy dispersive X-ray spectrometer (EDS). These microstructure measurements were carried out on magnetic extracts. One gram bulk sample and 0.1 g sodium hexametaphosphate were dispersed in 60 mL distilled water by ultrasonic vibrator for 20 min (He & Pan, 2020). The magnetic minerals were extracted using a neodymium-iron-boron magnet for 12 h. Magnetic extracts were placed onto a copper grid coated by carbon film for TEM analysis.

4. Results

4.1. XRD Analysis

Environmental magnetic parameters (*S*-ratio, a measure of the relative amounts of high-coercivity remanence to low-coercivity remanence, and -$IRM_{-0.3T}$, the absolute amount of low-coercivity remanence), loss-on-ignition (LOI), and chemical weathering indexes (molecular ratios of Silica-Titania Index [STI] 100*[SiO_2/TiO_2]/[SiO_2/TiO_2] + [SiO_2/Al_2O_3] + [Al_2O_3/TiO_2]) (Jayawardena & Izawa, 1994), SiO_2/Al_2O_3 (SA) (Nettleton & Kiek, 1966) and $SiO_2/(Al_2O_3 + Fe_2O_3)$ (SAF) (Ruxton, 1968), all display four weathering stages (Liu et al., 2020, 2021) designated D1, D2, D3, and D4 of the Damei sequence (Figure 2a). Selected samples from these four weathering stages were investigated by XRD analysis (Figure 2b). The intensity of the characteristic peaks of quartz is highest on the XRD spectrum of all the selected samples, indicating the abundance of quartz in the red soils. Kaolinite is the second abundant mineral of all the selected samples, which are typical in the red soils of south China (Yin & Guo, 2006). The concentration of kaolinite is much higher in G6-22 from Unit D3 (Figure 2b), which indicates much stronger chemical weathering (Bühmann, 1994; Chen & Wang, 2004). This is consistent with geochemical results (Figure 2a). The concentrations of illite are very high in Units D3 and D4. Illite always indicates semi-arid to arid soil environments (Allen & Hajek, 1989; Fanning et al., 1989). However, the high content of kaolinite in this section (Figure 2b) denotes a warm and wet climate, which coincides with the prevailing Quaternary climate in this tropical area (Yin & Guo, 2006; Yuan et al., 2008). This warm and wet environment is not favorable for the preservation of detrital illite. Therefore, illite is probably a pedogenic product of strong weathering rather than a detrital input. It is reported that illite can be transformed from smectite under cyclical wetting and drying (Deconinck et al., 1988), which can be used as an indication of seasonality (Huggett & Cuadros, 2005). The 14.7 Å peak of the D1 sample (Figure 2b) can be ascribed to the characteristic peak of illite/smectite mixed-layer clay as suggested by Hong et al. (2010). This illite/smectite may be the intermediate phase in the transformation from smectite to illite. High illite content in Units D3 and D4 suggests that these two units might be formed under intense alternating dry and wet climates. Clay mineral assemblages are different in each unit of the Damei sequence, which is in line with changing environments. Note that three magnetic minerals of goethite, hematite, and maghemite can be distinguished but hardly quantified on the XRD spectra (Figure 2b).

4.2. Magnetic Mineralogy

Thermal magnetic analyses are usually used to identify and characterize magnetic minerals. An intensity drop between 300 and 400°C on the χ–T and M_s–T heating curves and the thermal demagnetization curve of the soft

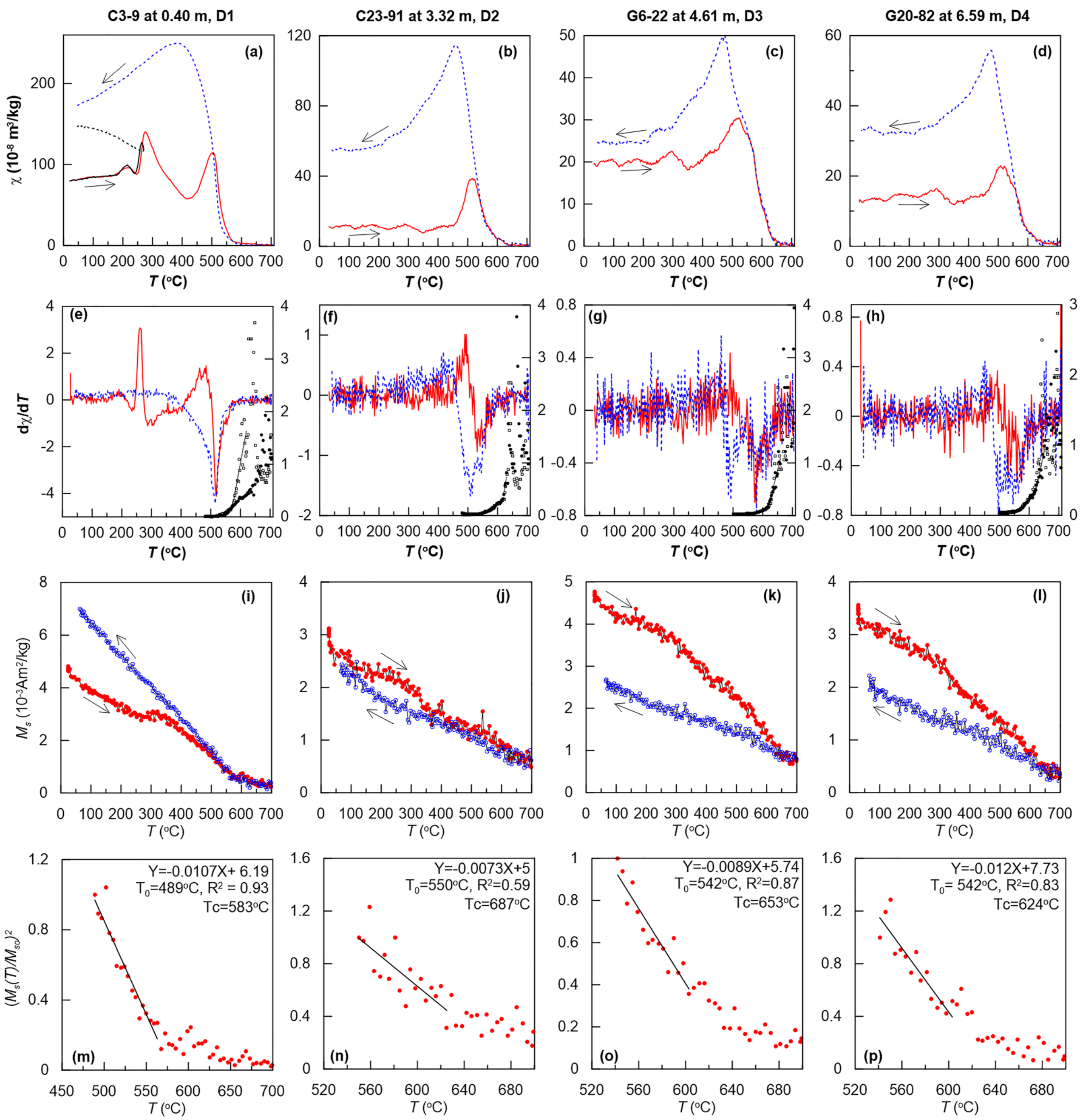

Figure 3. (a–d) High-temperature magnetic susceptibility ($\chi-T$ curves), (e–h) first-order derivative of (a–d) (red solid and blue dashed lines) and temperature dependence of inverse susceptibility ($1/\chi-T$ curves) in the high-temperature region (black circles), (i–l) high-temperature magnetization (M_s–T curves), and (m–p) T_c from M_s–T curves (i–l) using the extrapolating method (Moskowitz, 1981) of selected samples from the Damei four weathering stages. Red solid and blue dashed lines or red solid and blue hollow circles represent heating and cooling runs, respectively. Black solid/dashed lines in (a) represent heating/cooling curves of 270°C heating cycle. Black solid and hollow circles in (e–h) represent the heating and cooling data, respectively. Black thin lines in (e–h) are the best linear fits of $1/\chi-T$ curves. The data in (a–d), (i–j), and (l) come from (Deng et al., 2007; Liu et al., 2010, 2020). The extrapolating method (Moskowitz, 1981) is based on the quantum mechanical and thermodynamic aspects of the temperature variation of saturation magnetization near T_c. An equation, $(M_s(\mathrm{T})/M_{s0})^2 = T_c/(T_c - T_0) - T/(T_c - T_0)$, has been used to calculate T_c, where T_0 is the starting temperature value which we used to get the fitting line of $(M_s(\mathrm{T})/M_{s0})^2$ versus T. T_0 is usually 100°C lower than T_c. M_{s0} is the saturation magnetization at T_0.

fraction of the three-component IRM (Figures 3 and 4) suggest the presence of pedogenic fine-grained maghemite (Text S1–S3 in Supporting Information S1). All the three types of thermal-magnetic curves (χ–T, M_s–T and thermal demagnetization of three-component IRM) of D1 sample (Figures 3a, 3e, 3i, 3m, and 4a) display

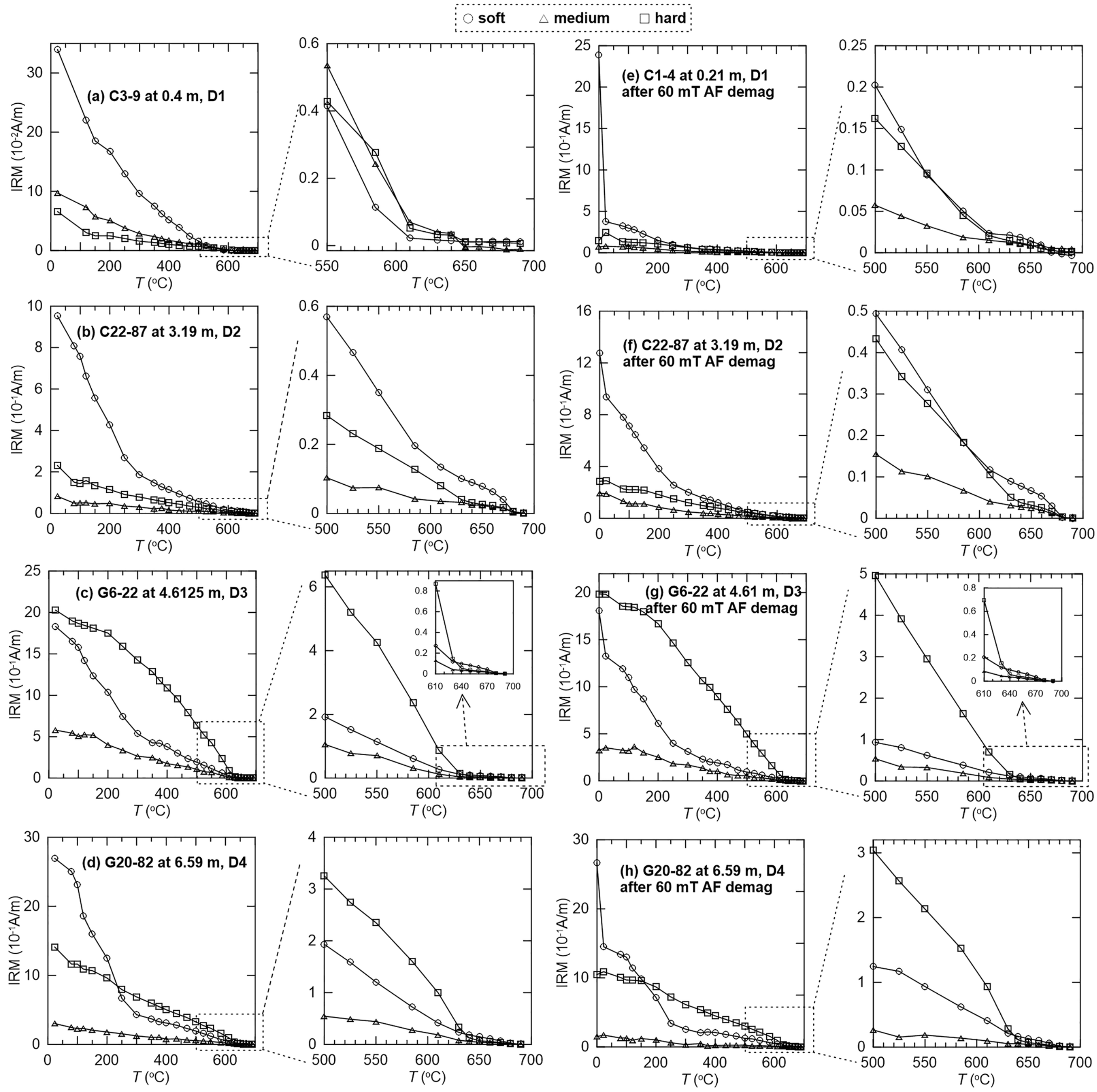

Figure 4. (a−d) Progressive thermal demagnetization of a three-component IRM (Lowrie, 1990) of selected samples from the Damei section. The composite IRM was obtained by magnetizing in successively smaller fields (2.7 T, 0.5 T, and 0.05 T) along mutually perpendicular *Z, Y,* and *X* axes, respectively. (e−h) Progressive thermal demagnetization of a three-component IRM (Lowrie, 1990), which is produced by magnetizing samples in successively smaller fields (2.7 T, 0.5 T, and 0.05 T) along the *Z, Y,* and *X* axes, respectively, and then demagnetized in an alternating field (AF) of 60 mT along the *Z, Y,* and *X* axes. The data at 0°C in (e–h) are the soft, medium and hard IRM values before the 60 mT AF demagnetization.

a significant inversion at 585°C, which indicates the presence of magnetite in unit D1. The χ–T curves of the selected D2, D3, and D4 samples display a nearly flat pattern below 400°C (Figures 3b–3d) suggesting that there may be coarse-grained maghemitized or partially oxidized magnetite (Text S1 in Supporting Information S1). Similar thermal demagnetization behavior of two types three-component IRM (the composite IRM that was not subjected to AF demagnetization and the composite IRM that was subjected to a 60 mT three-axis AF demagnetization), except for the decrease of soft fraction (Figure 4), indicates the T_B at around 640 and 680°C represent

10.1029/2021JB023165

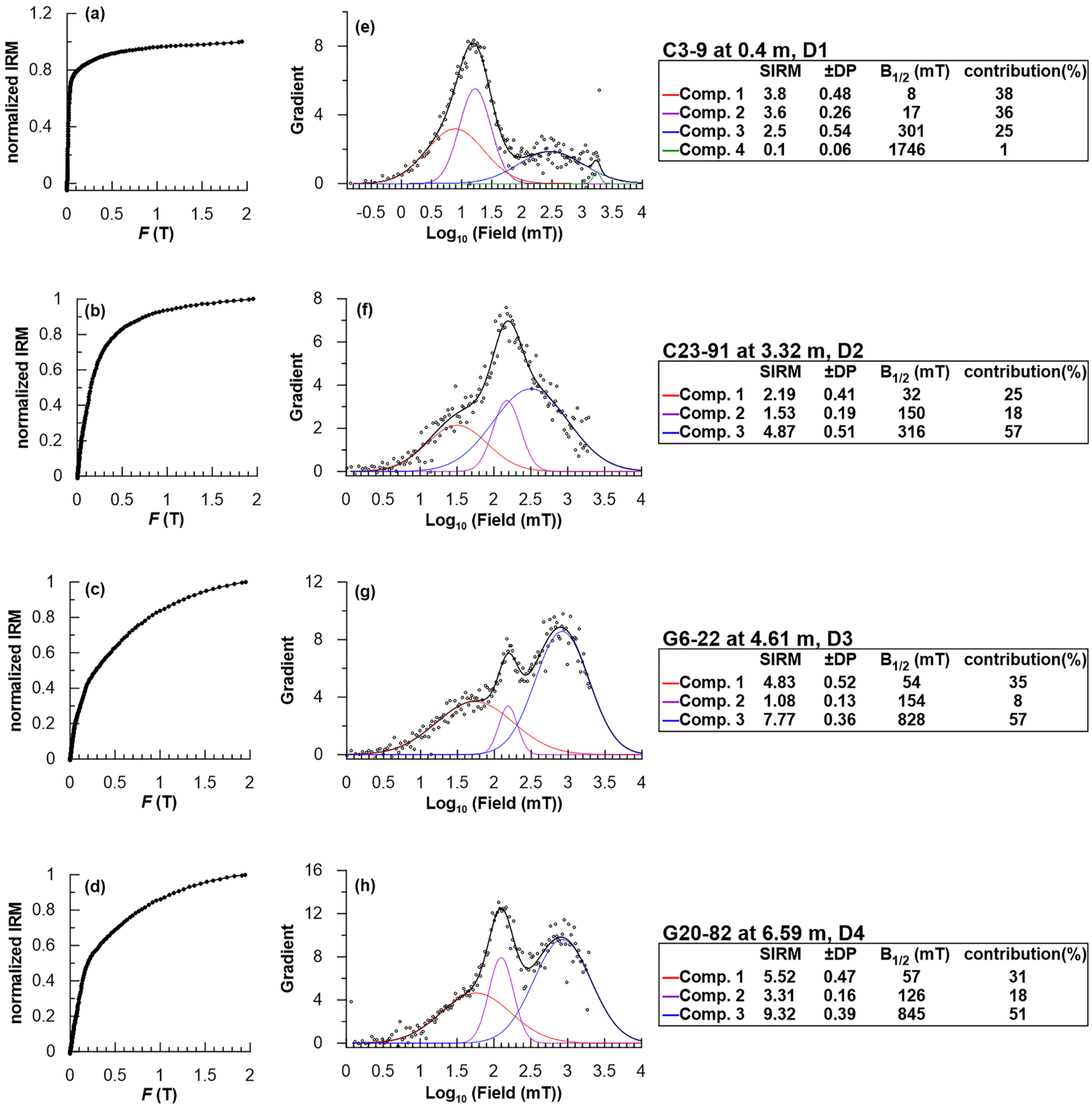

Figure 5. (a-d) IRM acquisition curves and (e-h) IRM component analyses. Red, purple, blue, and green curves represent different coercivity components derived from the coercivity spectra using GECA (Egli, 2004). Black lines are the sum of these components. Open circles indicate raw IRM gradient data. $B_{1/2}$, the field at which half of the SIRM is reached; DP, dispersion parameter.

pedogenic hematite with T_B of 630–640°C and specular hematite with T_B of 685°C, respectively (Text S3 in Supporting Information S1). The presence of goethite can be confirmed by the intensity drop at 80°C on the thermal demagnetization curves of medium and high fractions of the three-component IRM (Figure 4, Text S3 in Supporting Information S1).

Based on the above thermal-magnetic analyses (Text S1–S3 in Supporting Information S1), the components 1, 2, 3, and 4 on the coercivity spectrum of the D1 samples (Figure 5e) should correspond to fine-grained maghemite, magnetite, hematite, and goethite, respectively (Text S4 in Supporting Information S1). Components 1, 2, and 3 of the D2, D3, and D4 samples (Figures 5f–5h) represent ferrimagnetic magnetite/maghemite, fine-grained

10.1029/2021JB023165

specular hematite with T_B of 685°C, and pedogenic hematite with T_B of 630–640°C (Text S3 in Supporting Information S1).

4.3. Paleomagnetic Results

The PaleoMag software (Jones, 2002) was used for analyzing paleomagnetic results. Progressive thermal demagnetization results were displayed by vector component diagram (Zijderveld, 1967) (the left plots in Figure 6). The direction of each magnetic remanence component was computed by principal component analysis (Kirschvink, 1980). Three remanence components were derived from different temperature ranges of the orthogonal diagrams (Figures 6a–6d). The low-temperature (LT) components were resolved between 80/120°C and 200/300°C, the medium-temperature (MT) components, 300/350°C to 525/585°C, and the high-temperature (HT) components, the temperature range above 630°C (Figure 6a, 6b and 6d) or 525°C (Figure 6c).

Decay curves of the NRM (the middle plots in Figure 6) display a significant drop below 300°C. Nearly 80% intensity has been demagnetized below this temperature. The intensity of sample C5-19 (Figure 6a) shows a gradual decrease to 685°C. Unlike C5-19, the J/J_0 of other samples (Figures 6b and 6d) first continues to decrease until 525°C and then goes up till 610°C and then decreases again. For samples G9-31 (Figure 6c), these two magnetic intensity reversals occurred at lower temperatures (respectively at 450 and 525°C). Due to the weakness in magnetic intensity above 525°C and the neoformation of ferrimagnetic minerals and the inversion of maghemite to hematite during heating (Figure 3), the residual magnetic field of the furnace should be kept as low as possible. In this study, we used a newly designed thermal demagnetizer TD-PGL-100 with a special "straight core solenoid" which greatly reduces the residual field to less than 1 nT (Qin et al., 2020). Even with this precaution, we checked the influence of the residual field on weak remanence by changing the placement direction of each sample in the furnace in the next heating step. For example, we placed the *X*-axis of the sample oriented to the furnace inlet when heating to 585°C, while the *X*-axis of the sample oriented to the furnace offtake in the next heating step of 610°C. In that way, if the sample was remagnetized by the residual field in the furnace during heating, the remanence direction will vary regularly. Fortunately, this regular variation has not been found in our demagnetization results. However, the measurement error still disordered the demagnetization behavior of weak remanence, only 24 (45%) samples yielded the stable HT components. Least squares fits of the LT, MT, and HT components are summarized in equal-area projections (the right plots in Figure 6).

Quite different from the thermal demagnetization (Figure 6), the 100 mT AF demagnetization on the selected D2, D3, and D4 samples (Figures 7b–7d) cleaned off 20–60% of the original remanence. Only a low-field component can be constrained for these samples. Around 95% natural remanence of the selected D1 sample has been demagnetized by 100 mT AF (Figure 7a). Low-field and medium-field components of this sample have been discriminated and both are normal-polarity.

Virtual geomagnetic pole (VGP) latitudes were calculated from the declination and inclination of the remanence vector. The LT components display a normal polarity except for two points (Figures 8b–8e). These components should be the viscous remanence magnetized by the recent geomagnetic field. Both the MT and HT components (Figures 8f–8m) present a normal polarity in Unit D1. The MT components (Figures 8f–8i) show a reverse polarity between 0.8 and 1.2 m, while the HT components (Figure 8j–8m) display a normal polarity in the same depth range. A normal polarity was recorded by MT components below 1.2 m depth (Figures 8f–8i), but the polarity of the HT components is a little complex below that depth (Figures 8j–8m). The maximum angular deviations (MAD) of the LT components, except for two points, are lower than 10° (Figure 8d). The MAD of most MT components is lower than 15°, only two points are excluded (Figure 8h). Only four HT components have a MAD higher than 15° (Figure 8l).

4.4. DRS Results

DRS is sensitive to color and has been intensively applied on examining Fe oxides which are main soil pigments (Scheinost et al., 1998; Torrent & Barrón, 2002, 2008), especially to identify and semi-quantify goethite and hematite in soils (e.g., Ji et al., 2002; Jiang et al., 2014; Shen et al., 2006; Torrent & Barrón, 2003). The second-derivative curves of the Kubelka–Munk (K–M) remission function supply more information than original spectra (Scheinost et al., 1998; Torrent & Barrón, 2008). In this study, the second-derivative curves were used to semi-quantify goethite and hematite of each vermiculated red soil sample from the Damei, Xuancheng, and

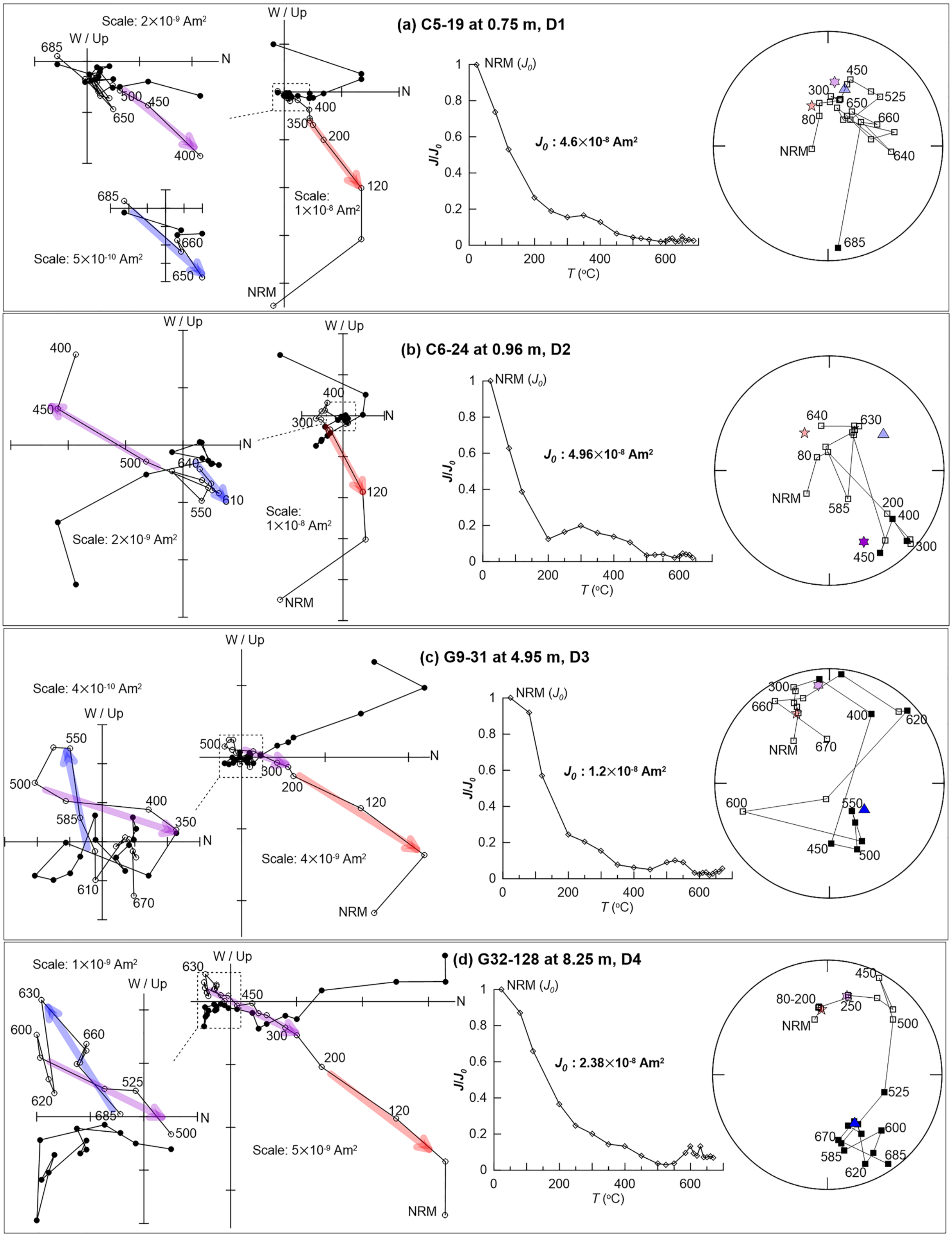

Figure 6. Orthogonal projections (left), magnetic remanence intensity curves (middle), and equal-area projections (right) of representative progressive thermal demagnetization in geographic coordinates for selected samples. The solid (open) circles represent magnetic vector points in the horizontal (vertical) planes. The numbers stand for the temperatures in °C of each point. NRM is the natural remanent magnetization. Red, purple and blue arrows respectively represent the low-temperature (LT), middle-temperature (MT), high-temperature (HT) components. Solid (open) squares in equal-area stand for upper (lower) –hemisphere directions. Red, purple and blue shapes in equal-area respectively represent least-squares fits of LT, MT, HT components.

10.1029/2021JB023165

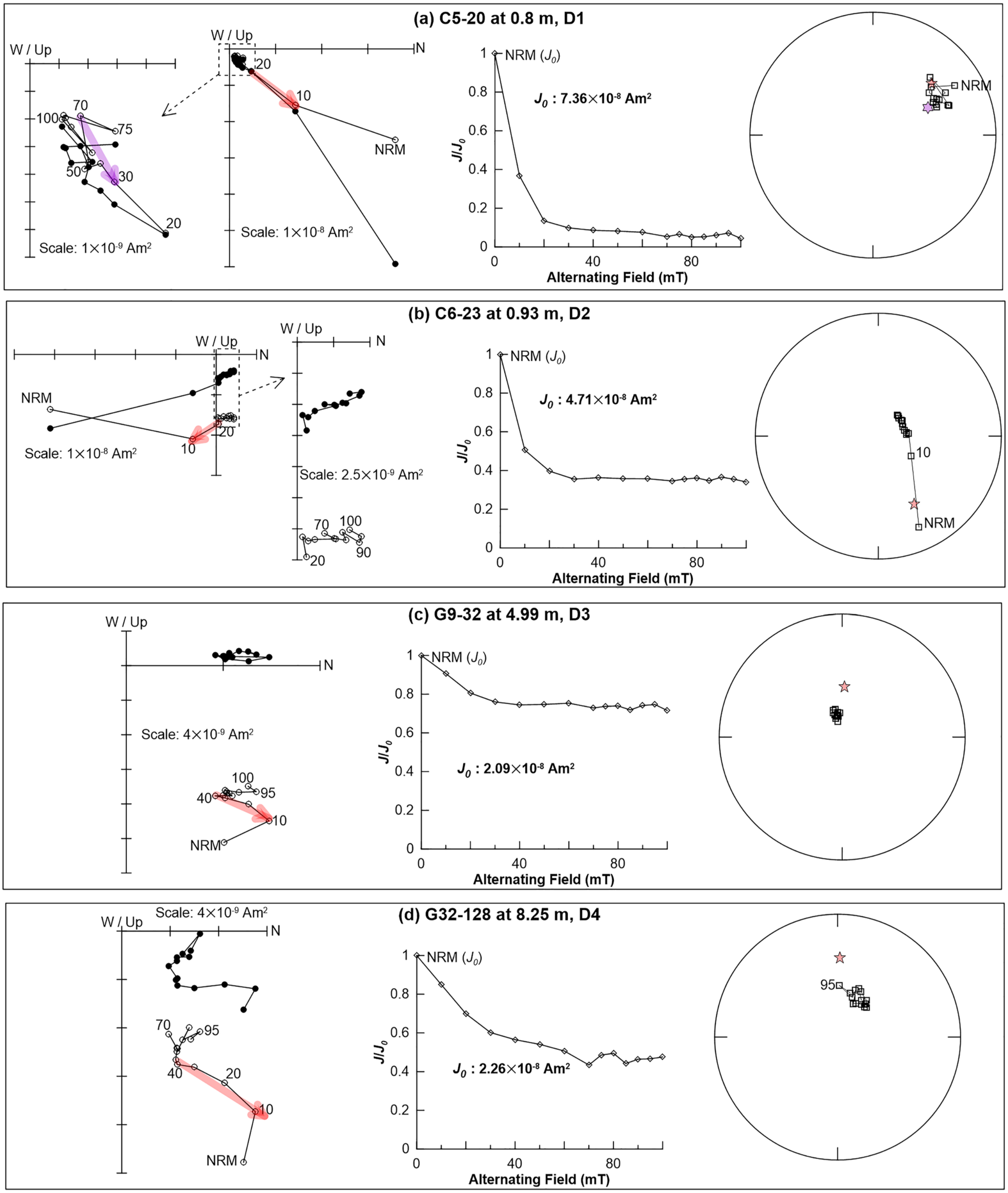

Figure 7. Orthogonal projections (left), magnetic remanence intensity curves (middle), and equal-area projections (right) of representative progressive alternating field (AF) demagnetization in geographic coordinates for selected samples. The solid (open) circles represent magnetic vector points in the horizontal (vertical) planes. The numbers stand for the alternating field in mT of each point. NRM is the natural remanent magnetization. Red and purple arrows respectively represent low and middle field components. Open squares in equal-area stand for lower–hemisphere directions. Red and purple shapes in equal-area respectively represent least-squares fits of low and middle field components.

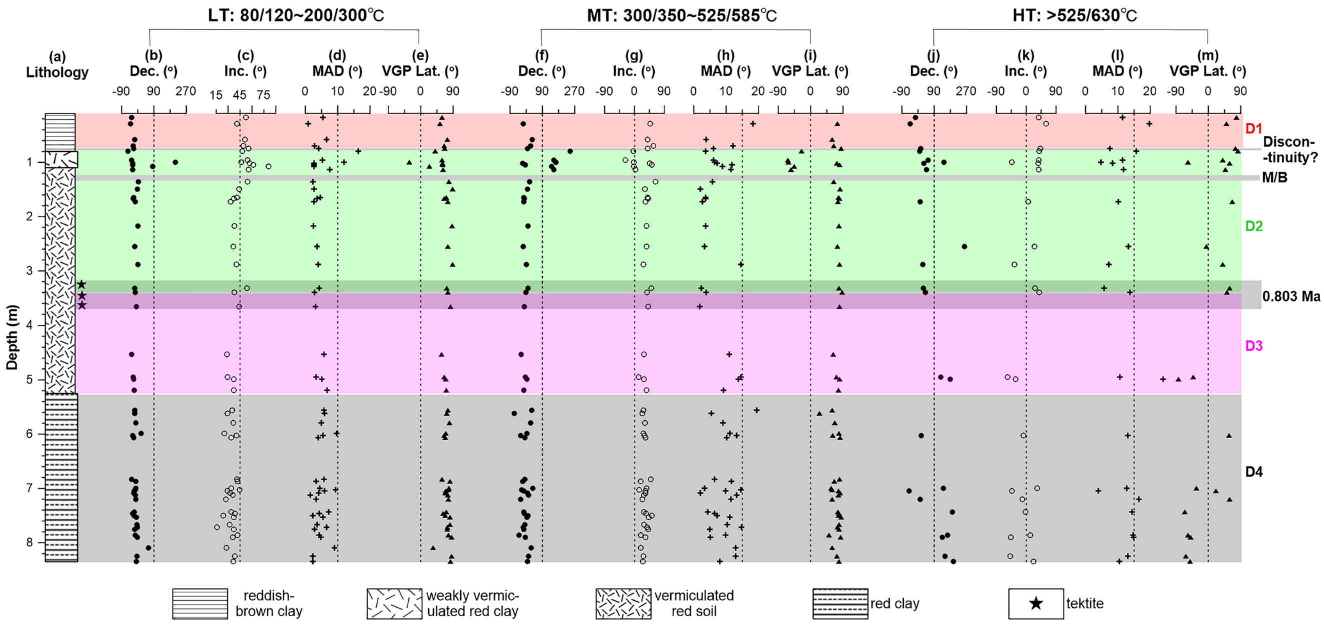

Figure 8. Lithostratigraphy (a) and magnetic polarity stratigraphy of the LT (b–e), MT (f–i) and HT (j–m) components. Dec., declination; Inc., inclination; MAD, maximum angular deviation; VGP Lat., the latitude of the virtual geomagnetic pole; M/B, Matuyama-Brunhes boundary.

Qiliting sequence (Figure 9a). DRS results indicate that the amplitudes between characteristic bands of goethite of the Damei samples are much higher than those of Xuancheng and Qiliting samples, however, the amplitudes of hematite are just the reverse.

4.5. TEM, SAED, and EDS Analyses

Maghemite and hematite crystals were distinguished by SAED patterns and high-resolution TEM imaging (Figure 10). Due to the influence of copper grid and analysis error, elements of C, Cu, and those with At% (atom percent) <1 should be excluded from the EDS results of iron oxides. Magnetic minerals usually attach to the particles of clay minerals. The magnetic extraction process could not completely remove the clay mineral. Therefore, Si and Al signal may come from the left clay minerals. However, a higher Al/Si ratio (0.26–3.28) in magnetic extracts than that (0.12–0.27) in bulk samples (Liu et al., 2021) suggests that Al-substitution might occur in these iron oxide crystals. Some iron oxide particle only contains Al but not Si (Figure 10b) further confirming the Al-substitution in iron oxide.

5. Discussion

5.1. Magnetic Carriers of the LT, MT, and HT Magnetic Remanence Components of the Damei Sequence

Magnetic mineralogy is substantially different in the four weathering stages of the Damei sequence defined in the previous section (Figure 2) as shown by the rock magnetic properties of each subunit (Figures 3–5, Text S1–S4 in Supporting Information S1). The relationship of magnetic parameters and geochemical weathering indices (Figure 2) suggests that the magnetic assemblage, particularly the magnetic remanence carriers, closely depend on in-situ weathering or pedogenesis. The small grain size (20–150 nm) of magnetic particles displayed in TEM images (Figure 10) further supports the pedogenic origin of most magnetic components. Based on the magnetic mineralogy analysis and the thermal demagnetization behavior of NRM, magnetic carriers of each magnetic remanence component (Figures 6 and 8) were summarized in Table 1.

The weakly weathered D1 samples (higher STI, SAF, and SA values of Unit D1 than the other three units in Figure 2) display bulk ferrimagnetic behavior, high magnetic susceptibility, and low magnetic coercivity, compared with the other units based on rock magnetic analysis (Figures 2–5, Table 1, Supporting Information S1). Magnetic mineralogy analyses (Figures 3a, 3e, 3i, 3m, 4a, 4e, 5a, and 5e, and Text S1–S4 in Supporting

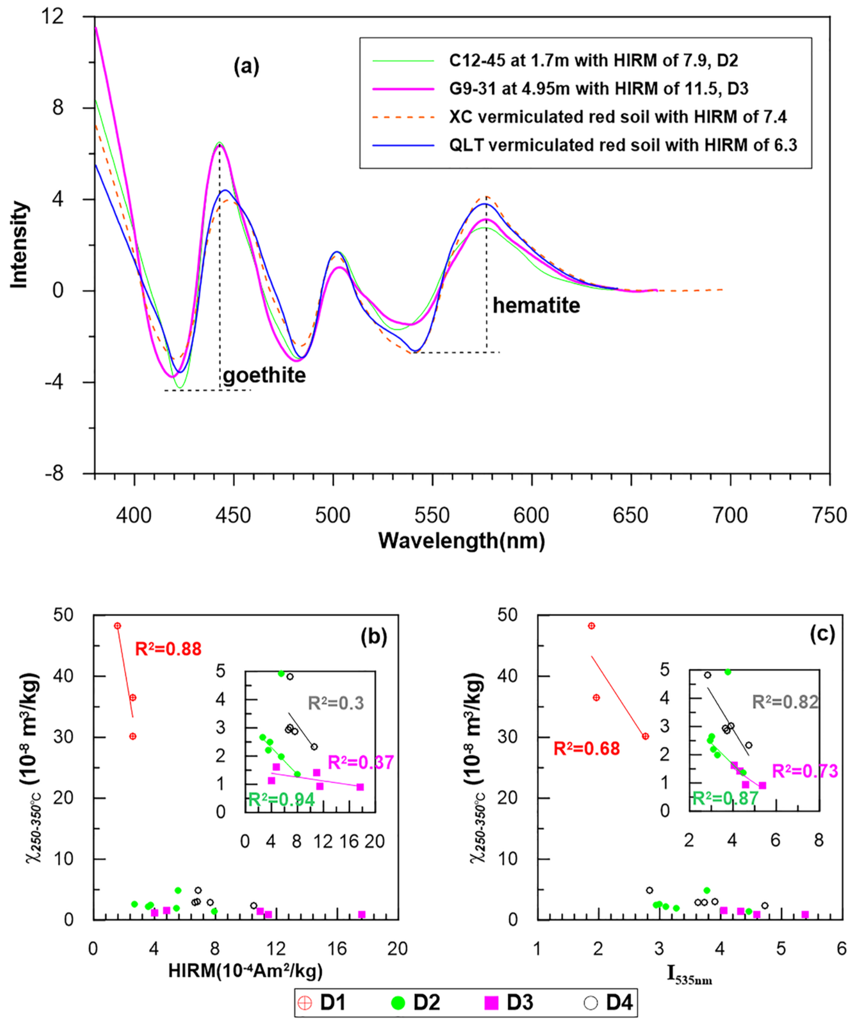

Figure 9. (a) The second-derivative curves of the K-M (Kubelka-Munk) function (Scheinost et al., 1998; Torrent & Barrón, 2008) were calculated from Diffuse Reflectance Spectroscopy (DRS) for selected samples from the Damei, Xuancheng, and Qiliting sequences. Goethite and hematite have been semi-quantified by the amplitude of the second-derivative curve band between the ~415 nm minimum and the 445 nm maximum, and that between the ~535 nm minimum and the 580 nm maximum (Scheinost et al., 1998). The original data of C12-45 and G9-31 have been published in (Liu et al., 2021). (b and c) Correlations between $\chi_{250\text{-}350°C}$ (Liu et al., 2020) and HIRM, I_{535nm} (Liu et al., 2021). $\chi_{250\text{-}350°C}$, a loss in χ between 250/300 and 350/400°C on the $\chi-T$ heating curves and indicating the concentration of pedogenic fine-grained maghemite. I_{535nm} varies with the hematite content.

Information S1) suggest that magnetite and pedogenic fine-grained maghemite are the main ferrimagnetic minerals in the D1 sample that contributes 74% of the total remanence (Figure 5e, Text S4 in Supporting Information S1). The remanence residuals after the 585°C thermal demagnetization and the 100 mT AF demagnetization are only 2% and 4% of the NRM (Figures 6a and 7a), which confirms that these two ferrimagnetic minerals dominate the demagnetization behavior of the LT and MT remanence components of the D1 sample (Figures 6a and 8b–8i). The natural remanence of the D1 sample displays a significant decrease at around 300°C (Figure 6a), which likely relates to the conversion of maghemite to hematite (Text S1–S3 in Supporting Information S1). It seems that the LT (80/120–200/300°C) remanence component is mainly carried by pedogenic fine-grained maghemite. Goethite is present (Figure 4a, Text S3 in Supporting Information S1) but contributes only 1% to the whole remanence (Figure 5e), so its contribution to LT is limited. The MT remanence component is observed between 300/350 and 525/585°C which corresponds to the unblocking range of magnetite. All the three fractions of the three-component IRM display the highest T_B at 680°C even after a 60 mT AF demagnetization (Figures 4a

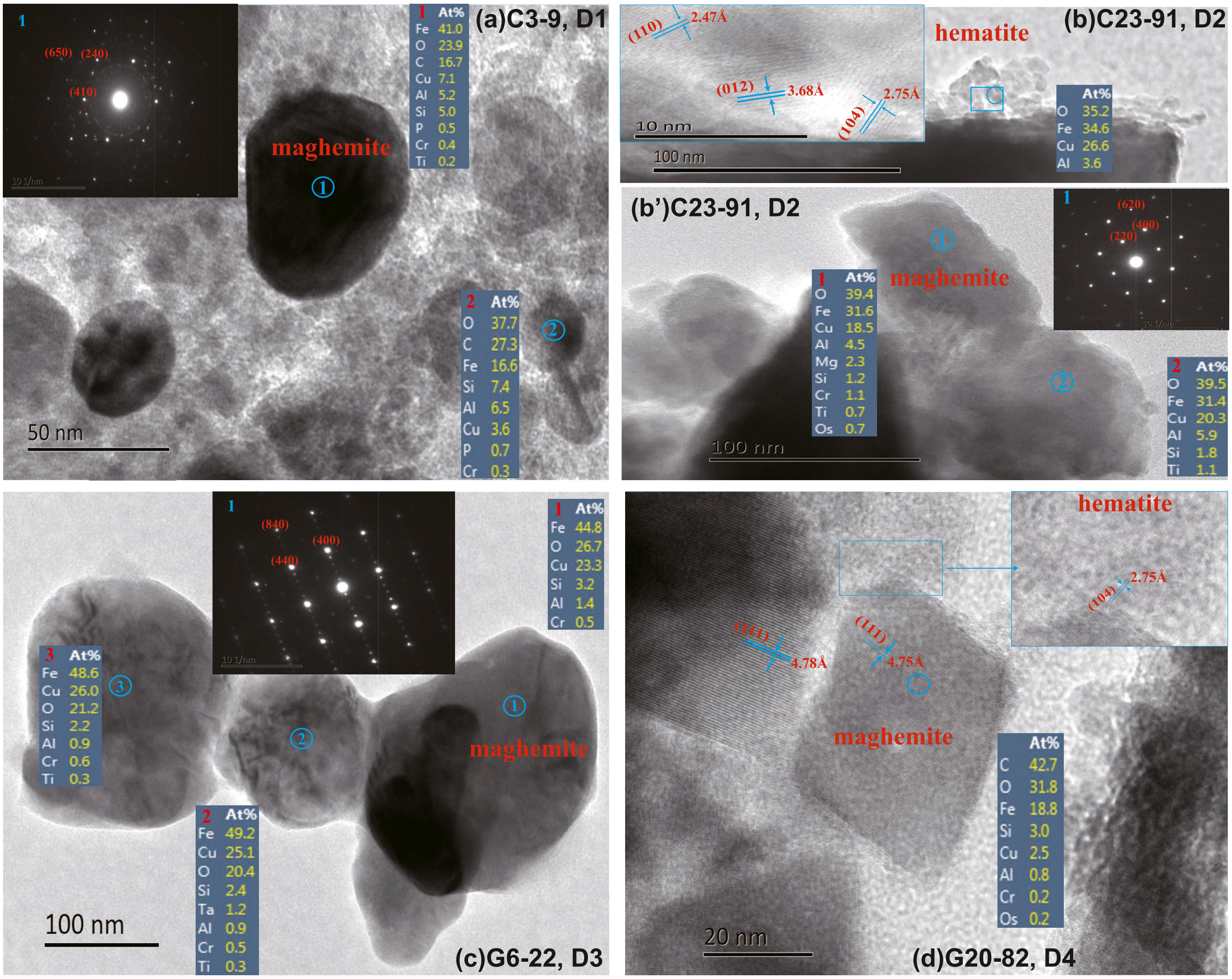

Figure 10. TEM images, SAED patterns, and EDS analysis results of magnetic extracts from the Damei sequence. The circle is the selected area for SAED and EDS analysis. The image in the blue rectangle in (b) is the high-resolution TEM image of the blue boxed region. SAED pattern in (a)–(c) indicating cubic crystal of maghemite. The spacing of lattice fringes in the bands between the blue lines is displayed in the unit of Å, which corresponds to the d-values (distance of the crystal plane) of hematite (b) and (d) and maghemite (d).

and 4e, Text S3 in Supporting Information S1). This suggests that the HT component observed between 650 and 685°C (Figures 6a and 8j–8m) is mainly carried by specular hematite with T_B of 685°C.

For the D2 samples, thermal magnetic analyses (Figures 3b, 3f, 3j, 3n, and 4b and 4f, Text S3 in Supporting Information S1) suggest the presence of pedogenic fine-grained maghemite, magnetite, pedogenic hematite with T_B of 630–640°C and specular hematite with T_B of 685°C. EDS analysis on the iron oxide particles (Figure 10) suggests that Al-substitution may occur in some iron oxides. The hematite with T_B around 640°C is more likely Al-substituted because Al-substitution can cause a decrease in T_B (Jiang et al., 2012; Wells et al., 1999). Similar to the D1 sample (Figure 6a), the D2 samples also display a large intensity decrease below 200–300°C (Figure 6b) which suggests the predominant contribution of pedogenic fine-grained maghemite to LT. Magnetite is identified on the demagnetization curve of soft fraction in Figures 4b and 4f (Text S3 in Supporting Information S1) and may be coarse-grained partially oxidized or maghemitized as suggested by $\chi-T$ analysis (Figure 3b, Text S1 in Supporting Information S1). However, the contribution of magnetite to the MT component of D2 sample could be limited, because the remanence intensity is nearly unchanged during 30–100 mT (coercivity range of coarse-grained magnetite) AF demagnetization (Figure 7b). This is further confirmed by identical behavior between 350 and 585°C of the thermal demagnetization curves of two types of composite IRM (one were not subjected to

10.1029/2021JB023165

Table 1
Magnetic Carrier of Each Remanence Component in the Four Damei Units

	Mean χ (10^{-8} m^3/kg)	Rem. comp.	Main magnetic carrier
Unit D1	65.75	LT	Pedogenic fine-grained maghemite
		MT	Magnetite
		HT	Hematite with T_B of 685°C
Unit D2	11.46	LT	Pedogenic fine-grained maghemite
		MT	Al-substituted hematite with T_B of 630–640°C (self-reversal, predominant), maghemitized or partially oxidized magnetite (limited contribution)
		HT	Specular hematite with T_B of 685°C
Unit D3	10.31	LT	Pedogenic fine-grained maghemite
		MT	Al-substituted hematite with T_B of 630–640°C (self-reversal), maghemitized or partially oxidized magnetite (limited contribution)
		HT	Specular hematite with T_B of 685°C
Unit D4	10.81	LT	Pedogenic fine-grained maghemite
		MT	Al-substituted hematite with T_B of 630–640°C (self-reversal, predominant), maghemitized or partially oxidized magnetite (contribute to inclination shallower)
		HT	Specular hematite with T_B of 685°C

an AF demagnetization and the other were subjected to a 60 mT AF demagnetization) (Figures 4b and 4f, Text S3 in Supporting Information S1). Therefore, the MT component defined between 350 and 585°C (Figures 6b and 8f–8i) should be mainly carried by Al-substituted hematite, which displays a significant unblocking below 610°C (Figures 4b and 4f, Text S3 in Supporting information). Also based on the thermal demagnetization behavior of the three-component IRM (Figures 4b and 4f, Text S3 in Supporting Information S1), the specular hematite with T_B of 685°C is the main carrier of the HT component (Figures 6b and 8j–8m).

Similar to the D1 and D2 samples, the LT components of the D3 and D4 samples (Figures 6c and 6d and 8b–8e) are mainly carried by pedogenic fine-grained maghemite. The pedogenic (Al-substituted) hematite with T_B around 640°C dominates the demagnetization behavior of all the three fractions of three-component IRM between 300 and 630°C (Figure 4c, 4d, 4g, and 4h, Text S3 in Supporting Information S1). This indicates that Al-substituted hematite should be the main carrier of MT components of D3 and D4 samples (Figures 6c and 6d and 8f–8i). A significant gap above 350°C between the M_s–T heating and cooling curve (Figure 3k and 3l) may be caused by inversion of maghemitized or partially oxidized magnetite to hematite at high temperature (Text S2 in Supporting Information S1). This kind of magnetite may also contribute to the MT remanence component of these samples (Figures 6c and 6d and 8f–8i). However, up to 72% of remanence residual after a 100 mT AF demagnetization for the D3 sample (Figure 7c) indicates that the contribution of partially oxidized magnetite to MT remanence is limited. For the D4 samples, the residual after a 100 mT AF demagnetization is 48% of the original NRM. The contribution of partially oxidized magnetite to MT remanence component cannot be neglected. Maybe this partially oxidized magnetite and Al-substituted hematite carried remanence with different polarity, which caused the shallowed inclination of Unit D4 compared with Units D2 and D3 (Figure 8g). For example, the reversed remanence carried by partially oxidized magnetite overlapped on the normal remanence of Al-substituted hematite. Due to the higher contribution of Al-substituted hematite than magnetite, the MT remanence component displays a normal polarity but shallowed inclination (Figure 8g). This inclination shallowing of Unit D4 is also found in our previous work (Deng et al., 2007). Similar to the D2 sample, the main carrier of HT components of the D3 and D4 samples (Figures 6c and 6d and 8j–8m) is specular hematite with T_B of 685°C. The intensity of the HT component of the D3 samples is too weak to be easily distinguished from the thermal demagnetization, so only two samples from this unit have a stable HT component.

Much lower mean χ values of Units D2, D3, and D4 than that of Unit D1 (Table 1) suggests the limited content of high magnetic ferrimagnetic minerals in Units D2, D3, and D4. A residual intensity of 40–70% of the NRM of Units D2, D3, and D4 after a 100 mT AF demagnetization (Figures 7b–7d; Liu et al., 2010) furtherly confirms that hard magnetic minerals are the main carriers of the NRM of these red soils. As the main remanence carrier (contribute 51–57% of the total remanence of Units D2, D3, and D4; Figures 5f–5h, Text S4 in Supporting Information S1), pedogenic Al-substituted hematite dominates the polarity of the MT remanence component. In addition, this hematite displays a higher coercivity in Units D3 and D4 (component 3 in Figures 5g and 5h) than that in Unit D2 (component 3 in Figure 5f) (Text S4 in Supporting Information S1). This corresponds to the higher illite content in D3 and D4 than that in D2 (Figure 2b). Illite here indicates a strong seasonal weathering (Huggett & Cuadros, 2005). It seems that seasonal weathering promotes the growth of large grain-sized Al-substituted hematite.

5.2. Self-Reversal of the MT Remanence Components due to the Transformation of Maghemite to Hematite

The magnetostratigraphy of the MT components (Figure 8i) displays a similar property to our previous results which yield only normal polarity between 1.7 and 8.35 m depth of the Damei sequence (Deng et al., 2007). This is inconsistent with the $^{40}Ar/^{39}Ar$ age (803 ± 3 ka) of tektite present in the depth interval between 3.2 and 3.7 m (Hou et al., 2000). The HT components display a normal polarity above 1.2 m and a predominantly reverse polarity below the tektite layer (Figure 8m) being consistent with the tektite age. The HT component seems to record the in-situ geomagnetic field polarity, and below the depth of 0.8 m (lower boundary of Unit D1, Figure 8) the MT component is reversed to it Figures(6b-6d and 8), except for a few points (Figure 8). Below we discuss the possible mechanism of the MT.

Based on the above rock mineral analysis, the main carrier of the MT components is Al-substituted hematite. This mineral is formed during pedogenesis and should carry a CRM. Several types of CRM exist. The most common one is acquired by grain growth of new-formed magnetic minerals (Tauxe, 2010), which can also be called "crystallization remanence" acquired by a crystal during its nucleation and growth (Haigh, 1958). There is another type of CRM, *alteration chemical remanence*, acquired by alteration of a preexisting mineral to a ferromagnetic mineral (Tauxe, 2010) or by a phase change from one magnetic mineral to another (Haigh, 1958). Our previous study (Liu et al., 2021) indicated that hematite in the Damei sequence was mainly transformed from maghemite. This interpretation is confirmed by the negative correlations between the *S*-ratios and chemical weathering indexes (Figure 2a), $\chi_{250–350°C}$ (indicating the content of pedogenic maghemite) (Liu et al., 2020) and HIRM (Figure 9b), $\chi_{250–350°C}$ and I_{235nm} (varies with hematite content) (Liu et al., 2021) (Figure 9c). Al-substituted hematite with coercivity larger than 300 mT, as suggested by analysis of coercivity distributions and three-component IRM demagnetization (Figures 4 and 5, Text S3 and S4 in Supporting Information S1), is undoubtedly the main carrier of HIRM. Therefore, the CRM carried by Al-substituted hematite is more like alteration chemical remanence.

During the transformation of maghemite to hematite, a special self-reversal phenomenon has been observed in some volcanic rocks (McClelland, 1987; Swanson-Hysell et al., 2011). It might occur by super-exchange coupling of the maghemite and hematite regions during the inversion process (McClelland & Goss, 1993). On inversion, the hematite phase is magnetized antiparallel to the internal field of the maghemite by super-exchange interactions between these two phases. The reversed MT components of the Damei sequence look like a self-reversal of CRM. During the in-situ weathering process, pedogenic maghemite first formed which developed during a penecontemporaneous stage, acquired a remanence parallel to the external geomagnetic field. Following further pedogenesis, maghemite transformed to hematite and at the same time hematite acquired a magnetization anti-parallel to that of the maghemite by super-exchange interactions. Under the strong weathering, maghemite has been largely depleted and the quantity of pedogenic hematite increased and finally predominates the remanence of the Damei sequence. Although there are no reports about the self-reversed record in red sediments, the self-reversal CRM has previously been found in hematite transformed from maghemite by heating in the lab (Hedley, 1968; McClelland & Goss, 1993). In McClelland and Goss (1993) experiment, the maghemite was produced by the dehydration of synthetic lepidocrocite and then transformed to hematite by heating. This process is common in the pedogenesis of red soils (Liu et al., 2012, 2021; Torrent et al., 2006; Wang et al., 2013). Maghemite and hematite are common minerals in red soils, as well as the Damei section (Figures 3–5).

Our previous research indicated that the transformation of maghemite to hematite was also developed in the vermiculated red soils of Xuancheng and Qiliting sequences in the lower reaches of the Yangtze River (Figure 1) (Liu et al., 2012), whereas paleomagnetic field has been faithfully recorded in these sequences (Liu et al., 2008, 2010). Self-reversal has not been found in the experiment of acquiring CRM during the transformation from ferrihydrite to hematite in an Earth-like magnetic field (Jiang et al., 2015). The self-reversal of CRM on the transformation of maghemite to hematite does not systematically occur. McClelland and Goss (McClelland & Goss, 1993) have found that this self-reversal is only observed when the maghemite is in suitable grain size or a special microstructure. We noticed that the pedogenic hematite from the Damei sequence has lower T_B and higher coercivity compared with that from the Xuancheng and Qiliting sequences (Liu et al., 2010).

It is reported that Al-substitution can cause an increase in coercivity but a decrease in T_B of hematite (Jiang et al., 2012; Wells et al., 1999). Al content in soils of the Bose Basin is much higher than these sequences in the lower reaches of the Yangtze River due to stronger weathering in Damei (Yin & Guo, 2006; Yuan et al., 2008). High Al content usually favors the Al substitution in pedogenic magnetic mineral crystals (Jiang & Liu, 2012). Al-substitution in iron oxides is very normal in laterites (Fitzpatrick & Schwertmann, 1982; Herbilion & Nahon, 1988; Schwertmann et al., 1977; Tardy & Nahon, 1985). The intensity of the characteristic peak of hematite on the DRS spectra of the Damei vermiculated samples is weaker than that from the Xuancheng and Qiliting sequences, which is inconsistent with higher HIRM values of the Damei samples than others (Figure 9a). This may be caused by the Al-substitution in pedogenic hematite of the Damei sequence, because Al-substitution can cause the decrease in amplitude of the characteristic absorption band of hematite on the DRS and XRD spectra due to crystallinity decrease of hematite (Liu, Torrent, et al., 2011; Schwertmann et al., 1977; Torrent & Barrón, 2003). EDS analysis (Figure 10) further confirms that Al-substitution occurs in iron oxides grains of the Damei sequence.

Self-reversal on the transformation of maghemite to hematite has been thought to be produced by interactions across the maghemite-hematite phase boundary and the larger the surface area between the phases, the stronger the interactions (McClelland & Goss, 1993). It is reported that Al-substitution maghemite displays a larger surface area per unit mass than pure maghemite (Sidhu, 1988; Wells et al., 1999). In addition, Al-substitution can postpone the transformation from maghemite to hematite (Sidhu, 1988; Wells et al., 1999). That means it will need more time or a higher temperature to finish the transformation (Sidhu, 1988; Wells et al., 1999). More time or higher temperature benefits for growing larger maghemite particles. Coarse-grained maghemite is relatively more stable and likely keep blocked during the transformation, which favors the production of self-reversal of CRM on the transformation of maghemite to hematite because self-reversal of hematite remanence more likely occurs when the parent maghemite is still blocked during its transformation to hematite (McClelland & Goss, 1993). Al-substitution largely influenced the paleomagnetic records of the Damei sequence. Due to relatively weak weathering in the lower reaches of the Yangtze River (Figure 1), Al-substitution is limited in the Xuancheng and Qiliting sequences, therefore self-reversal has not affected these two sequences.

Similarly, self-reversal also cannot happen in specular hematite with T_B of 685°C. Therefore, the fine-grained specular hematite (maybe directly transformed from ferrihydrite; Jiang et al., 2018) of the Damei section record an HT component being parallel to the paleo-geomagnetic field (Figures 6 and 8), which is reverse to the MT components carried by Al-substituted hematite with T_B of 640°C at the depth interval of 0.8–8.3 m (Figures 6b–6d, 8). However, due to the low concentration and weakly magnetic property of this specular hematite, just a few samples get stable HT components. Some samples have an HT component with the same polarity as the MT component, especially at the depth interval of 1.2–3.4 m (Figure 8), which may be caused by the overlap of MT components to HT components. The predominant Al-substituted hematite even makes an effect on the LT components. Some nano-sized Al-substituted hematite may unblock at low temperature (<300°C), but the high coercivity caused by Al-substitution makes it record the same direction as the MT component. This component overlapped to the viscous remanence carried by fine-grained low-coercivity ferrimagnetic maghemite and caused the shallowing in inclination of the LT components between the depth of 1.2 and 8.35 m (<45°) (Figure 8c).

Based on the above analysis, the HT components should be a reliable recorder of the paleomagnetic field. However, due to the weakness in remanence intensity of these components, they are hard to be completely distinguished and cannot be used to build complete and continuous magnetostratigraphy of the Damei sequence. Although the MT components were self-reversed, the stability and high intensity of these components can correctly define the location of the Matuyama-Brunhes boundary (Figure 8). The sudden change in magnetic mineralogy (Figures 3–5, Text S1-S4 in Supporting Information S1), clay mineral composition (Figure 2b), and soil color between Units D1 and D2 suggest that there may be a sedimentary discontinuity between these two units (Figure 8).

Although only two previous works have identified the self-reversal of CRM on the transformation of maghemite to hematite (McClelland, 1987; Swanson-Hysell et al., 2011), the antiparallel component in red beds have been observed many times (e.g., Kruiver et al., 2003; Lee et al., 1996; Rösler et al., 1997; Tauxe et al., 1980; Turner et al., 1984). Some of them attributed the antiparallel directions between two components derived from different temperature ranges to later remagnetization after deposition (Tauxe et al., 1980). The self-reversal mechanism should be considered. It needs additional attention to deal with the CRM records of red soils in which the transformation of maghemite to hematite is observed, especially for those with Al-substitution.

6. Conclusions

The Damei red soil sequence in the subtropical (climate zone at present) Bose Basin consists of four weathering stages (D1, D2, D3, and D4), based on the geochemical, and clay mineral analyses. Progressive thermal demagnetization measurements up to 685°C carried out on the Damei samples reveal LT, MT, and HT magnetic remanence components. These remanence components were derived from different temperature ranges. Detailed rock magnetic analyses suggest that the main carrier of the LT components is fine-grained maghemite, which carried the viscous remanence recording the direction of the recent magnetic field. The magnetic carrier of the MT components is different between Unit D1 and other units. For Unit D1, magnetite is the main carrier of the MT component, which displays the same normal polarity as the HT component. The MT components of Units D2, D3, and D4 mainly carried by Al-substituted hematite with T_B of 640°C, were self-reversed (reverse to the HT component), which formed during the transformation of maghemite to hematite. Al-substitution may postpone the transformation of fine-grained maghemite to hematite and make the transformation occurred in coarse-grained maghemite, which favors the self-reversal of CRM on the transformation. The HT components carried by specular hematite with T_B of 685°C can be used to construct reliable magnetic polarity stratigraphy of the red soil sequence in the Bose Basin. Nevertheless, self-reversal should be considered when studying the natural remanence carried by Al-substituted hematite, especially for strongly weathered red soils.

Data Availability Statement

All data in this article are available in the Zenodo database (https://doi.org/10.5281/zenodo.6354842).

Acknowledgments

The Editor, Dr. Mark Dekkers, and Dr. Erwin Appel and one anonymous reviewer are deeply appreciated for their insightful comments and suggestions, which have significantly improved the manuscript. All measurements were made in the Institute of Geology and Geophysics, Chinese Academy of Sciences. The authors thank Dr. Tang Xu for his efforts to maintain smooth operation in TEM experiments. Xie Hao is appreciated for his help on some rock magnetic measurements. Financial assistance was provided by the National Natural Science Foundation of China grants 42074077 and 41888101, the Second Tibetan Plateau Scientific Expedition and Research (STEP) Grant 2019QZKK0704, and the National Key R&D Program of China Grant 2017YFC1500104.

References

Allen, B., & Hajek, B. (1989). Mineral occurrence in soil environments. *Minerals in soil environments (mineralsinsoile)*, 199–278. https://doi.org/10.2136/sssabookser1.2ed.c5

Bühmann, C. (1994). Parent material and pedogenic processes in South Africa. *Clay Minerals*, *29*(2), 239–246. https://doi.org/10.1180/claymin.1994.029.2.09

Chen, J., & Wang, H. N. (2004). *Geochemistry: Geochemistry of weathering*. Science Press.

Collinson, D. (1965). The remanent magnetization and magnetic properties of red sediments. *Geophysical Journal International*, *10*(1), 105–126. https://doi.org/10.1111/j.1365-246X.1965.tb03055.x

Collinson, D. (1966). Carrier of remanent magnetization in certain red sandstones. *Nature*, *210*(5035), 516–517. https://doi.org/10.1038/210516a0

Collinson, D. (1974). The role of pigment and specularite in the remanent magnetism of red sandstones. *Geophysical Journal International*, *38*(2), 253–264. https://doi.org/10.1111/j.1365-246X.1974.tb04119.x

Deconinck, J., Strasser, A., & Debrabant, P. (1988). Formation of illitic minerals at surface temperatures in Purbeckian sediments (Lower Berriasian, Swiss and French Jura). *Clay Minerals*, *23*(1), 91–103. https://doi.org/10.1180/claymin.1988.023.1.09

Deng, C. L., Liu, Q. S., Wang, W., & Liu, C. C. (2007). Chemical overprint on the natural remanent magnetization of a subtropical red soil sequence in the Bose Basin, southern China. *Geophysical Research Letters*, *34*(22). https://doi.org/10.1029/2007GL031400

Egli, R. (2003). Analysis of the field dependence of remanent magnetization curves. *Journal of Geophysical Research: Solid Earth*, *108*(B2). https://doi.org/10.1029/2002JB002023

Egli, R. (2004). Characterization of individual rock magnetic components by analysis of remanence curves, 1. Unmixing natural sediments. *Studia Geophysica et Geodaetica*, *48*(2), 391–446. https://doi.org/10.1023/B:SGEG.0000020839.45304.6d

Fanning, D. S., Keramidas, V. Z., & El-Desoky, M. A. (1989). *Micas*. Soil Science Society of America Madison. https://doi.org/10.2136/sssabookser1.2ed.c12

Fitzpatrick, R. W., & Schwertmann, U. (1982). Al-substituted goethite—An indicator of pedogenic and other weathering environments in South Africa. *Geoderma*, *27*(4), 335–347. https://doi.org/10.1016/0016-7061(82)90022-2

Glennie, K. W. (1970). *Desert sedimentary environments*. Elsevier.

Haigh, G. (1958). The process of magnetization by chemical change. *Philosophical Magazine*, *3*(27), 267–286. https://doi.org/10.1080/14786435808238219

He, K., & Pan, Y. (2020). Magnetofossil abundance and diversity as paleoenvironmental proxies: A case study from Southwest Iberian Margin sediments. *Geophysical Research Letters*, *47*(8). https://doi.org/10.1029/2020GL087165

Hedley, I. (1968). Chemical remanent magnetization of the FeOOH, Fe2O3 system. *Physics of the Earth and Planetary Interiors*, *1*(2), 103–121. https://doi.org/10.1016/0031-9201(68)90055-1

Herbilion, A. J., & Nahon, D. (1988). Laterites and laterization processes. *Iron in Soils and Clay Minerals*. https://doi.org/10.1007/978-94-009-4007-9_22

Hong, H., Gu, Y., Li, R., Zhang, K., & Li, Z. (2010). Clay mineralogy and geochemistry and their palaeoclimatic interpretation of the Pleistocene deposits in the Xuancheng section, southern China. *Journal of Quaternary Science*, *25*(5), 662–674. https://doi.org/10.1002/jqs.1340

Hou, Y., Richard, P., Yuan, B., Zhengtang, G., Deino, A., Wei, W., et al. (2000). Mid-pleistocene Acheulean-like stone technology of the Bose Basin, south China. *Science*, *287*(5458), 1622–1626. https://doi.org/10.1126/science.287.5458.1622

Huggett, J., & Cuadros, J. (2005). Low-temperature illitization of smectite in the late Eocene and early Oligocene of the Isle of Wight (Hampshire basin), UK. *American Mineralogist*, *90*(7), 1192–1202. https://doi.org/10.2138/am.2005.1674

Jayawardena, U. d. S., & Izawa, E. (1994). A new chemical index of weathering for metamorphic silicate rocks in tropical regions: A study from Sri Lanka. *Engineering Geology*, *36*(3–4), 303–310. https://doi.org/10.1016/0013-7952(94)90011-6

Ji, J., Balsam, W., Chen, J., & Liu, L. (2002). Rapid and quantitative measurement of hematite and goethite in the Chinese loess-paleosol sequence by diffuse reflectance spectroscopy. *Clays and Clay Minerals*, *50*(2), 208–216. https://doi.org/10.1346/000986002760832801

Jiang, Z., & Liu, Q. (2012). Factors controlling the Al content in Al-substituted hematite and its environmental significances. *Quaternary Sciences*, *32*(4), 608–614. https://doi.org/10.3969/j.issn.1001-7410.2012.04.05

Jiang, Z., Liu, Q., Barrón, V., Torrent, J., & Yu, Y. (2012). Magnetic discrimination between Al-substituted hematites synthesized by hydrothermal and thermal dehydration methods and its geological significance. *Journal of Geophysical Research: Solid Earth*, *117*(B2). https://doi.org/10.1029/2011JB008605

Jiang, Z., Liu, Q., Colombo, C., Barrón, V., Torrent, J., & Hu, P. (2014). Quantification of Al-goethite from diffuse reflectance spectroscopy and magnetic methods. *Geophysical Journal International*, *196*(1), 131–144. https://doi.org/10.1093/gji/ggt377

Jiang, Z., Liu, Q., Dekkers, M. J., Tauxe, L., Qin, H., Barrón, V., & Torrent, J. (2015). Acquisition of chemical remanent magnetization during experimental ferrihydrite–hematite conversion in Earth-like magnetic field—Implications for paleomagnetic studies of red beds. *Earth and Planetary Science Letters*, *428*, 1–10. https://doi.org/10.1016/j.epsl.2015.07.024

Jiang, Z., Liu, Q., Dekkers, M. J., Zhao, X., Roberts, A. P., Yang, Z., et al. (2017). Remagnetization mechanisms in Triassic red beds from South China. *Earth and Planetary Science Letters*, *479*, 219–230. https://doi.org/10.1016/j.epsl.2017.09.019

Jiang, Z., Liu, Q., Roberts, A. P., Barrón, V., Torrent, J., & Zhang, Q. (2018). A new model for transformation of ferrihydrite to hematite in soils and sediments. *Geology*, *46*(11), 987–990. https://doi.org/10.1130/G45386.1

Jiang, Z., Liu, Q., Roberts, A. P., Dekkers, M. J., Barrón, V., Torrent, J., & Li, S. (2022). The magnetic and color reflectance properties of hematite: From Earth to Mars. *Reviews of Geophysics*, e2020RG000698. https://doi.org/10.1029/2020RG000698

Jones, C. H. (2002). User-driven integrated software lives: "Paleomag" paleomagnetics analysis on the Macintosh. *Computers & Geosciences*, *28*(10), 1145–1151. https://doi.org/10.1016/S0098-3004(02)00032-8

Jones, G. (1965). Red beds in northeastern Nigeria. *Sedimentology*, *5*(3), 235–247. https://doi.org/10.1111/j.1365-3091.1965.tb02114.x

Kirschvink, J. (1980). The least-squares line and plane and the analysis of palaeomagnetic data. *Geophysical Journal International*, *62*(3), 699–718. https://doi.org/10.1111/j.1365-246X.1980.tb02601.x

Kruiver, P. P., Dekkers, M. J., & Heslop, D. (2001). Quantification of magnetic coercivity components by the analysis of acquisition curves of isothermal remanent magnetisation. *Earth and Planetary Science Letters*, *189*(3), 269–276. https://doi.org/10.1016/S0012-821X(01)00367-3

Kruiver, P. P., Langereis, C. G., Dekkers, M. J., & Krijgsman, W. (2003). Rock-magnetic properties of multicomponent natural remanent magnetization in alluvial red beds (NE Spain). *Geophysical Journal International*, *153*(2), 317–332. https://doi.org/10.1046/j.1365-246X.2003.01880.x

Lee, Y., Nishimura, S., & Min, K. (1996). High-unblocking-temperature haematite magnetizations of Late Palaeozoic red beds from the Okcheon zone, southern part of the Korean Peninsula. *Geophysical Journal International*, *125*(1), 266–284. https://doi.org/10.1111/j.1365-246X.1996.tb06550.x

Liu, C., Deng, C., & Liu, Q. (2012). Mineral magnetic studies of the vermiculated red soils in southeast China and their paleoclimatic significance. *Palaeogeography, Palaeoclimatology, Palaeoecology*, *329*, 173–183. https://doi.org/10.1016/j.palaeo.2012.02.035

Liu, C., Deng, C., Liu, Q., Zheng, L., Wang, W., Xu, X., et al. (2010). Mineral magnetism to probe into the nature of palaeomagnetic signals of subtropical red soil sequences in southern China. *Geophysical Journal International*, *181*(3), 1395–1410. https://doi.org/10.1111/j.1365-246X.2010.04592.x

Liu, C., Dupont-Nivet, G., Deng, C., & Wang, W. (2021). Magnetic response to pedogenesis in aerobic soils of different weathering degree. *Palaeogeography, Palaeoclimatology, Palaeoecology*, *567*, 110240. https://doi.org/10.1016/j.palaeo.2021.110240

Liu, C., Ge, K., Zhang, C., Liu, Q., Deng, C., & Zhu, R. (2011). Nature of remagnetization of Lower Triassic red beds in southwestern China. *Geophysical Journal International*, *187*(3), 1237–1249. https://doi.org/10.1111/j.1365-246X.2011.05196.x

Liu, C., Wang, W., & Deng, C. (2020). A new weathering indicator from high-temperature magnetic susceptibility measurements in an Argon atmosphere. *Geophysical Journal International*, *221*(3), 2010–2025. https://doi.org/10.1093/gji/ggaa128

Liu, C., Xu, X., Yuan, B., & Deng, C. (2008). Magnetostratigraphy of the Qiliting section (SE China) and its implication for geochronology of the red soil sequences in southern China. *Geophysical Journal International*, *174*(1), 107–117. https://doi.org/10.1111/j.1365-246X.2008.03814.x

Liu, Q., Torrent, J., Barrón, V., Duan, Z., & Bloemendal, J. (2011). Quantification of hematite from the visible diffuse reflectance spectrum: Effects of aluminium substitution and grain morphology. *Clay Minerals*, *46*(1), 137–147. https://doi.org/10.1180/claymin.2011.046.1.137

Lowrie, W. (1990). Identification of ferromagnetic minerals in a rock by coercivity and unblocking temperature properties. *Geophysical Research Letters*, *17*(2), 159–162. https://doi.org/10.1029/GL017i002p00159

McClelland, E. (1987). Self-reversal of chemical remanent magnetization: A palaeomagnetic example. *Geophysical Journal International*, *90*(3), 615–625. https://doi.org/10.1111/j.1365-246X.1987.tb00744.x

McClelland, E., & Goss, C. (1993). Self reversal of chemical remanent magnetization on the transformation of maghemite to haematite. *Geophysical Journal International*, *112*(3), 517–532. https://doi.org/10.1111/j.1365-246X.1993.tb01185.x

Millot, G. v., Transby Far-rand, W. R., & Paquet, H. (1970). *Geology of clays* (p. 429). Springer-Verlag.

Moskowitz, B. M. (1981). Methods for estimating Curie temperatures of titanomaghemites from experimentalJs-T data. *Earth and Planetary Science Letters*, *53*(1), 84–88. https://doi.org/10.1016/0012-821X(81)90028-5

Nettleton, A. F., & Kiek, S. N. (1966). The significance of silica sesquioxide ratio in weathering of pavement materials - A review paper. *Paper presented at Australian Road Research Board Conference Proc*.

Oliver, G., & Prave, A. (2013). Palaeogeography of late Triassic red-beds in Singapore and the Indosinian Orogeny. *Journal of Asian Earth Sciences*, *76*, 214–224. https://doi.org/10.1016/j.jseaes.2013.01.022

Qin, H., Zhao, X., Liu, S., Paterson, G. A., Jiang, Z., Cai, S., et al. (2020). An ultra-low magnetic field thermal demagnetizer for high-precision paleomagnetism. *Earth Planets and Space*, *72*(1), 170. https://doi.org/10.1186/s40623-020-01304-0

Robertson, D., & France, D. (1994). Discrimination of remanence-carrying minerals in mixtures, using isothermal remanent magnetisation acquisition curves. *Physics of the Earth and Planetary Interiors*, *82*(3), 223–234. https://doi.org/10.1016/0031-9201(94)90074-4

Rösler, W., Metzler, W., & Appel, E. (1997). Neogene magnetic polarity stratigraphy of some fluviatile Siwalik sections, Nepal. *Geophysical Journal International*, *130*(1), 89–111. https://doi.org/10.1111/j.1365-246X.1997.tb00990.x

Ruhe, R. V. (1967). *Geomorphic surfaces and surficial deposits in southern New Mexico*.

Ruxton, B. P. (1968). Measures of the degree of chemical weathering of rocks. *The Journal of Geology*, 518–527. https://doi.org/10.1086/627357

Scheinost, A., Chavernas, A., Barrón, V., & Torrent, J. (1998). Use and limitations of second-derivative diffuse reflectance spectroscopy in the visible to near-infrared range to identify and quantify Fe oxide minerals in soils. *Clays and Clay Minerals*, *46*(5), 528–536. https://doi.org/10.1346/CCMN.1998.0460506

Schwertmann, U., Fitzpatrick, R., & Le Roux, J. (1977). Al substitution and differential disorder in soil hematites. *Clays and Clay Minerals*, *25*(5), 373–374. https://doi.org/10.1346/CCMN.1977.0250504

Shen, Z., Cao, J., Zhang, X., Arimoto, R., Ji, J., Balsam, W., et al. (2006). Spectroscopic analysis of iron-oxide minerals in aerosol particles from northern China. *The Science of the Total Environment*, *367*(2–3), 899–907. https://doi.org/10.1016/j.scitotenv.2006.01.003

Sidhu, P. (1988). Transformation of trace element-substituted maghemite to hematite. *Clays and Clay Minerals*, *36*(1), 31–38. https://doi.org/10.1346/CCMN.1988.0360105

Spassov, S., Heller, F., Kretzschmar, R., Evans, M., Yue, L., & Nourgaliev, D. (2003). Detrital and pedogenic magnetic mineral phases in the loess/palaeosol sequence at Lingtai (Central Chinese Loess Plateau). *Physics of the Earth and Planetary Interiors*, *140*(4), 255–275. https://doi.org/10.1016/j.pepi.2003.09.003

Swanson-Hysell, N. L., Feinberg, J. M., Berquó, T. S., & Maloof, A. C. (2011). Self-reversed magnetization held by martite in basalt flows from the 1.1-billion-year-old Keweenawan rift, Canada. *Earth and Planetary Science Letters*, *305*(1–2), 171–184. https://doi.org/10.1016/j.epsl.2011.02.053

Tardy, Y., & Nahon, D. (1985). Geochemistry of laterites, stability of Al-goethite, Al-hematite, and Fe3+-kaolinite in bauxites and ferricretes: An approach to the mechanism of concretion formation. *American Journal of Science*, *285*(10), 865–903. https://doi.org/10.2475/ajs.285.10.865

Tauxe, L. (2010). *Essentials of paleomagnetism*. University of California Press. https://doi.org/10.1525/9780520946378

Tauxe, L., Kent, D. V., & Opdyke, N. D. (1980). Magnetic components contributing to the NRM of Middle Siwalik red beds. *Earth and Planetary Science Letters*, *47*(2), 279–284. https://doi.org/10.1016/0012-821X(80)90044-8

Torrent, J., & Barrón, V. (2002). Diffuse reflectance spectroscopy of iron oxides. *Encyclopedia of Surface and Colloid Science*, (*1*), 1438–1446

Torrent, J., & Barrón, V. (2003). The visible diffuse reflectance spectrum in relation to the color and crystal properties of hematite. *Clays and Clay Minerals*, *51*(3), 309–317. https://doi.org/10.1346/CCMN.2003.0510307

Torrent, J., & Barrón, V. (2008). Diffuse reflectance spectroscopy. *Methods of Soil Analysis. Part*, *5*, 367–387.

Torrent, J., Barrón, V., & Liu, Q. (2006). Magnetic enhancement is linked to and precedes hematite formation in aerobic soil. *Geophysical Research Letters*, *33*(2). https://doi.org/10.1029/2005GL024818

Turner, P., Clemmey, H., & Flint, S. (1984). Palaeomagnetic studies of a Cretaceous molasse sequence in the central Andes (Coloso formation, northern Chile). *Journal of the Geological Society*, *141*(5), 869–876. https://doi.org/10.1144/gsjgs.141.5.0869

Van Houten, F. B. (1973). Origin of red beds: A review-1961-1972. *Annual Review of Earth and Planetary Sciences*, *1*, 39. https://doi.org/10.1146/annurev.ea.01.050173.000351

Walker, T. R. (1967). Formation of red beds in modern and ancient deserts. *Geological Society of America Bulletin* (Vol. *78*, pp. 353–368). https://doi.org/10.1130/0016-7606(1967)78[353:FORBIM]2.0.CO;2

Walker, T. R. (1974). Formation of red beds in moist tropical climates: A hypothesis. *Geological Society of America Bulletin*, *85*(4), 633–638. https://doi.org/10.1130/0016-7606(1974)852.0.CO

Wang, S., Lin, S., & Lu, S. (2013). Rock magnetism, iron oxide mineralogy and geochemistry of Quaternary red Earth in central China and their paleopedogenic implication. *Palaeogeography, Palaeoclimatology, Palaeoecology*, *379*, 95–103. https://doi.org/10.1016/j.palaeo.2013.04.010

Wang, W., Bae, C. J., Huang, S., Huang, X., Tian, F., Mo, J., et al. (2014). Middle Pleistocene bifaces from Fengshudao (Bose Basin, Guangxi, China). *Journal of Human Evolution*, *69*, 110–122. https://doi.org/10.1016/j.jhevol.2013.11.002

Wang, W., Mo, J., & Huang, Z. (2008). Recent discovery of handaxes associated with tektites in the Nanbanshan locality of the Damei site, Bose basin, Guangxi, South China. *Chinese Science Bulletin*, *53*(6), 878–883. https://doi.org/10.1007/s11434-008-0134-7

Wells, M., Fitzpatrick, R. W., Gilkes, R., & Dobson, J. (1999). Magnetic properties of metal-substituted haematite. *Geophysical Journal International*, *138*(2), 571–580. https://doi.org/10.1046/j.1365-246X.1999.00840.x

Yin, Q. Z., & Guo, Z. T. (2006). Mid-Pleistocene vermiculated red soils in southern China as an indication of unusually strengthened East Asian monsoon. *Chinese Science Bulletin*, *51*(2), 213–220. https://doi.org/10.1007/s11434-005-0490-5

Yuan, B., Xia, Z., Li, B., Qiao, Y., Gu, Z., Zhang, J., et al. (2008). Chronostratigraphy and stratigraphic division of red soil in southern China (in Chinese with English abstract). *Quaternary Sciences*, *28*(1), 1–13. https://doi.org/10.3321/j.issn:1001-7410.2008.01.001

Yuan, J., Yang, Z., Deng, C., Krijgsman, W., Hu, X., Li, S., et al. (2021). Rapid drift of the Tethyan Himalaya terrane before two-stage India-Asia collision. *National Science Review*, *8*(7), nwaa173. https://doi.org/10.1093/nsr/nwaa173

Zijderveld, J. (1967). In D. Collinson, K. Creer, & S. Runcorn (Eds.), AC demagnetization of rocks: Analysis of results. *Methods in paleomagnetism* (pp. 254–286). Elsevier.

References From the Supporting Information

Dekkers, M. (1989). Magnetic properties of natural goethite-I. Grain-size dependence of some low-and high-field related rockmagnetic parameters measured at room temperature. *Geophysical Journal International*, *97*(2), 323–340. https://doi.org/10.1111/j.1365-246X.1989.tb00504.x

Deng, C., He, H., Pan, Y., & Zhu, R. (2013). Chronology of the terrestrial upper Cretaceous in the Songliao basin, northeast Asia. *Palaeogeography, Palaeoclimatology, Palaeoecology*, *385*, 44–54. https://doi.org/10.1016/j.palaeo.2012.07.028

Deng, C.-l., Zhu, R.-X., Jackson, M., Verosub, K., & Singer, M. (2001). Variability of the temperature-dependent susceptibility of the Holocene eolian deposits in the Chinese loess plateau: A pedogenesis indicator. *Physics and Chemistry of the Earth - Part A: Solid Earth and Geodesy*, *26*(11), 873–878. https://doi.org/10.1016/S1464-1895(01)00135-1

Dunlop, D. J., & Özdemir, Ö. (1997). *Rock magnetism: Fundamentals and frontiers*. Cambridge University Press.

Egli, R. (2004). Characterization of individual rock magnetic components by analysis of remanence curves, 1. Unmixing natural sediments. *Studia Geophysica et Geodaetica*, *48*(2), 391–446. https://doi.org/10.1023/B:SGEG.0000020839.45304.6d

Eyre, J. (1996). The application of high resolution IRM acquisition to the discrimination of remanence carriers in Chinese loess. *Studia Geophysica et Geodaetica*, *40*(3), 234–242. https://doi.org/10.1007/BF02300740

France, D., & Oldfield, F. (2000). Identifying goethite and hematite from rock magnetic measurements of soils and sediments. *Journal of Geophysical Research: Solid Earth*, *105*(B2), 2781–2795. https://doi.org/10.1029/1999JB900304

Gao, X., Hao, Q., Oldfield, F., Bloemendal, J., Deng, C., Wang, L., et al. (2019). New high-temperature-dependence-of-magnetic-susceptibility-based climofunction for quantifying paleoprecipitation from Chinese loess. *Geochemistry, Geophysics, Geosystems*, *20*(8), 4273–4291. https://doi.org/10.1029/2019GC008401

Gehring, A., & Hofmeister, A. (1994). The transformation of lepidocrocite during heating: A magnetic and spectroscopic study. *Clays and Clay Minerals*, *42*(4), 409–415. https://doi.org/10.1346/CCMN.1994.0420405

Hanesch, M., Stanjek, H., & Petersen, N. (2006). Thermomagnetic measurements of soil iron minerals: The role of organic carbon. *Geophysical Journal International*, *165*(1), 53–61. https://doi.org/10.1111/j.1365-246X.2006.02933.x

Herbilion, A. J., & Nahon, D. (1988). *Laterites and laterization processes, iron in soils and clay minerals*, https://doi.org/10.1007/978-94-009-4007-9_22

Hu, P., Liu, Q., Torrent, J., Barrón, V., & Jin, C. (2013). Characterizing and quantifying iron oxides in Chinese loess/paleosols: Implications for pedogenesis. *Earth and Planetary Science Letters*, *369*, 271–283. https://doi.org/10.1016/j.epsl.2013.03.033

Jeleńska, M., Hasso-Agopsowicz, A., & Kopcewicz, B. (2010). Thermally induced transformation of magnetic minerals in soil based on rock magnetic study and Mössbauer analysis. *Physics of the Earth and Planetary Interiors*, *179*(3–4), 164–177. https://doi.org/10.1016/j.pepi.2009.11.004

Jiang, Z., Liu, Q., Barrón, V., Torrent, J., & Yu, Y. (2012a). Magnetic discrimination between Al-substituted hematites synthesized by hydrothermal and thermal dehydration methods and its geological significance. *Journal of Geophysical Research: Solid Earth*, *117*(B2). https://doi.org/10.1029/2011JB008605

Liu, C., Deng, C., Liu, Q., Zheng, L., Wang, W., Xu, X., et al. (2010). Mineral magnetism to probe into the nature of palaeomagnetic signals of subtropical red soil sequences in southern China. *Geophysical Journal International*, *181*(3), 1395–1410. https://doi.org/10.1111/j.1365-246X.2010.04592.x

Liu, C., Wang, W., & Deng, C. (2020). A new weathering indicator from high-temperature magnetic susceptibility measurements in an Argon atmosphere. *Geophysical Journal International*, *221*(3), 2010–2025. https://doi.org/10.1093/gji/ggaa128

Liu, Q., Deng, C., Yu, Y., Torrent, J., Jackson, M. J., Banerjee, S. K., & Zhu, R. (2005). Temperature dependence of magnetic susceptibility in an argon environment: Implications for pedogenesis of Chinese loess/palaeosols. *Geophysical Journal International*, *161*(1), 102–112. https://doi.org/10.1111/j.1365-246X.2005.02564.x

Lowrie, W. (1990). Identification of ferromagnetic minerals in a rock by coercivity and unblocking temperature properties. *Geophysical Research Letters*, *17*(2), 159–162. https://doi.org/10.1029/GL017i002p00159

Maher, B. A., Karloukovski, V., & Mutch, T. (2004). High-field remanence properties of synthetic and natural submicrometre haematites and goethites: Significance for environmental contexts. *Earth and Planetary Science Letters*, *226*(3–4), 491–505. https://doi.org/10.1016/j.epsl.2004.05.042

Oches, E. A., & Banerjee, S. K. (1996). Rock-magnetic proxies of climate change from loess-paleosol sediments of the Czech Republic. *Studia Geophysica et Geodaetica*, *40*(3), 287–300. https://doi.org/10.1007/BF02300744

Özdemir, Ö., & Dunlop, D. J. (1993). Chemical remanent magnetization during γFeOOH phase transformations. *Journal of Geophysical Research: Solid Earth*, *98*(B3), 4191–4198. https://doi.org/10.1029/92JB02569

Petrovský, E., & Kapička, A. (2006). On determination of the Curie point from thermomagnetic curves. *Journal of Geophysical Research: Solid Earth*, *111*(B12). https://doi.org/10.1029/2006JB004507

Spassov, S., Heller, F., Kretzschmar, R., Evans, M., Yue, L., & Nourgaliev, D. (2003). Detrital and pedogenic magnetic mineral phases in the loess/palaeosol sequence at Lingtai (Central Chinese Loess Plateau). *Physics of the Earth and Planetary Interiors*, *140*(4), 255–275. https://doi.org/10.1016/j.pepi.2003.09.003

Stacey, F., & Banerjee, S. K. (1974). *The physical principles of rock magnetism*. Elsevier.

Tauxe, L. (2010). *Essentials of paleomagnetism*, Univ of California Press, Berkeley. https://doi.org/10.1525/9780520946378

Tauxe, L., Kent, D. V., & Opdyke, N. D. (1980). Magnetic components contributing to the NRM of Middle Siwalik red beds. *Earth and Planetary Science Letters*, *47*(2), 279-284. https://doi.org/10.1016/0012-821X(80)90044-8

Van Oorschot, I., Dekkers, M., & Havlicek, P. (2002). Selective dissolution of magnetic iron oxides with the acid-ammonium-oxalate/ferrous-iron extraction technique—II. Natural loess and palaeosol samples. *Geophysical Journal International*, *149*(1), 106–117. https://doi.org/10.1046/j.1365-246X.2002.01641.x